11. SITE 970[1]

Shipboard Scientific Party[2]

HOLE 970A

Date occupied: 17 April 1995

Date departed: 19 April 1995

Time on hole: 2 days, 02 hr, 30 min

Position: 33°44.194′N, 24°48.120′E

Bottom felt (drill-pipe measurement from rig floor, m): 2086.9

Distance between rig floor and sea level (m): 11.4

Water depth (drill-pipe measurement from sea level, m): 2075.5

Total depth (from rig floor, m): 2288.3

Penetration (m): 201.4

Number of cores (including cores having no recovery): 22

Total length of cored section (m): 201.4

Total core recovered (m): 50.5

Core recovery (%): 25.0

Oldest sediment cored:
Depth (mbsf): 201.40
Nature: nannofossil clay, gravel, sand, and mud
Earliest age: late Pliocene
Measured velocity (km/s): 2.7

HOLE 970B

Date occupied: 19 April 1995

Date departed: 19 April 1995

Time on hole: 09 hr

Position: 33°44.214′N, 24°48.694′E

Bottom felt (drill-pipe measurement from rig floor, m): 2099.0

Distance between rig floor and sea level (m): 11.4

Water depth (drill-pipe measurement from sea level, m): 2078.6

Total depth (from rig floor, m): 2146.5

Penetration (m): 47.5

Number of cores (including cores having no recovery): 5

Total length of cored section (m): 47.5

Total core recovered (m): 48.7

Core recovery (%): 102.5

Oldest sediment cored:
Depth (mbsf): 47.50
Nature: nannofossil ooze
Earliest age: early Pleistocene
Measured velocity (km/s): 1.7

HOLE 970C

Date occupied: 19 April 1995

Date departed: 20 April 1995

Time on hole: 06 hr, 45 min

Position: 33°44.134′N, 24°47.457′E

Bottom felt (drill-pipe measurement from rig floor, m): 2048.3

Distance between rig floor and sea level (m): 11.4

Water depth (drill-pipe measurement from sea level, m): 2036.9

Total depth (from rig floor, m): 2083.9

Penetration (m): 35.6

Number of cores (including cores having no recovery): 5

Total length of cored section (m): 35.6

Total core recovered (m): 17.0

Core recovery (%): 47.0

Oldest sediment cored:
Depth (mbsf): 35.60
Nature: matrix-supported clast-rich debris-flow deposits

HOLE 970D

Date occupied: 20 April 1995

Date departed: 20 April 1995

Time on hole: 04 hr, 45 min

Position: 33°44.042′N, 24°46.613′E

Bottom felt (drill-pipe measurement from rig floor, m): 1964.7

Distance between rig floor and sea level (m): 11.4

Water depth (drill-pipe measurement from sea level, m): 1953.3

Total depth (from rig floor, m): 2007.5

Penetration (m): 42.8

Number of cores (including cores having no recovery): 5

Total length of cored section (m): 42.8

Total core recovered (m): 44.2

Core recovery (%): 103.2

Oldest sediment cored:
Depth (mbsf): 42.80
Nature: matrix-supported clast-rich debris-flow deposits

Principal results: A transect of four holes was drilled across the Milano mud structure on the northern flank of the Mediterranean Ridge to test alternate hypotheses for its origin as either a diapiric or a mud volcano structure. Moving toward the crest of the mud structure, the holes were drilled in the following order: Hole 970B, Hole 970A, Hole 970C, and Hole 970D. Hole 970B was drilled as a control through deep-sea sediments away from the mud structure. Typical hemipelagic sediments were recovered there, together with silts and sands that are interpreted as shed off the crestal area

[1]Emeis, K.-C., Robertson, A.H.F., Richter, C., et al., 1996. *Proc. ODP, Init. Repts.*, 160: College Station, TX (Ocean Drilling Program).
[2]Shipboard Scientific Party is given in the list preceding the Table of Contents.

by turbidity currents. Recovery at Hole 970A, on the outer flank of the mud structure, comprises alternations of mud debris flows and normal pelagic sediments at the top. Pebbly mudstones, with a thin pelagic intercalation, are underlain by thick clast-rich mud debris flows and then by further pelagic sediment. This, in turn, is followed by coarse-grained clastic sediments and by further pelagic sediments. Logging with the Formation MicroScanner also revealed an additional clastic interval below the lowest level cored. In addition, two holes were drilled on the crestal areas of the volcano (Holes 970C and 970D) and recovered mousselike (i.e., gaseous) muddy and silty sediments, with evidence of gas hydrates.

The most common facies are mud- and clast-rich, matrix-supported breccia/conglomerates ("mud breccias" of previous workers), interpreted as debris flows. Clastic intercalations were deposited partly as high-density turbidites. The matrix of the debris flows ranges from silt to sand and includes nannofossils, foraminifers, clay, quartz, and rock fragments. Clasts range from angular to locally rounded and comprise mainly claystone and siliciclastic sandstone, with some limestone. All the clasts are of Miocene age and were derived from metamorphic and plutonic igneous source areas, possibly represented by rocks exposed on Crete today.

The flank holes show a strong increase in salinity with depth, which is explained by the upward diffusion of brine from underlying, presumably Messinian, evaporites. However, at the flank sites pore-water salinities decrease markedly with depth, which is explained by the presence of clathrates (methane hydrates) at shallow levels. In addition, methane is present at one of the crestal sites (Hole 970D).

In conclusion, the Milano structure is interpreted as a mud volcano that became active at about 1.74 Ma or earlier, based on micropaleontological dating.

BACKGROUND AND OBJECTIVES

Site 970 was the first of two transects drilled across two well-known examples of mud mounds, interpreted as mud volcanoes, or mud diapirs, both of which are located within the Olimpi mud diapir field (see "Tectonic Introduction" chapter, this volume). The structure drilled is known as the Milano "diapir" (Camerlenghi et al., 1995; Fig. 1). It is several kilometers in diameter and rises approximately 80 m above the surrounding seafloor (see "Site Geophysics" section, this chapter). The Milano structure is unusual in that single-channel sparker lines reveal dipping seismic reflectors around the edge of the structure that could be interpreted as the result of interfingering of materials (i.e., flows or sills) with surrounding deep-sea sediments. If such interdigitation could be cored and dated, it could reveal the age of the volcano and information on processes of mud mound construction. Alternate hypotheses for the formation of these mud structures are, first, that they are relatively rigid pluglike structures that were emplaced vertically upward as diapirs, and second, they could be mud volcanoes that were constructed by up-piling of semifluid debris flows fed from a central vent, in a manner similar to land volcanic cones. In reality, it is probable that these deep-sea mud structures experienced several phases of development, in which both "diapirism" and "volcanism" may play a role. Previous studies have not revealed any evidence that the Milano structure is currently active (i.e., releasing fluid, sediment, or gases) and for this reason it offered an opportunity to make a comparison with the Napoli mud dome drilled at Site 971, which is known to be currently active.

The most appropriate strategy to enable characterization of the anatomy of the Milano mud mound was to drill a transect of four holes from the flanks to the crest of the structure, in the following spatial order: Hole 970B, Hole 970A, Hole 970C, and Hole 970D.

Hole 970B was sited on the seafloor directly adjacent to the mud mound in an attempt the define the overall size of the mud mound structure. Hole 970A was located on the outer flank of the volcano. Seismic interpretation suggested that a layer of material derived from the mud mound, perhaps mud flows, might be underlain by normal Pleistocene and/or Pliocene sediments. This site could thus record the timing of the onset of volcanism and any evidence of disturbance of the underlying sediments. Hole 970C was sited at the base of the slope of the mud structure. In the subsurface, seismic reflectors dip sharply inward and suggest that a moatlike structure could have formed from a phase of collapse of the core area of the structure, perhaps akin to the phenomenon of caldera collapse in terrestrial volcanoes. The "moat" could be infilled with mud debris flows, or mud sills, and thus record a history of eruption and/or intrusion. Hole 970D (restricted to 50 m of penetration) was located on the crest of the mud structure. The main objective was to determine if distinctive intruded or extruded material forms the core of the volcano (e.g., of pluglike origin) and if there is evidence that the structure is currently active (based on temperature and pore-fluid studies).

In summary, the objectives of drilling on the Milano mud structure were (1) to determine its age and three-dimensional anatomy; (2) to infer the modes of mud mound construction, including the expulsion of pluglike material, extrusion of mud debris flows, or intrusion of mud sills; (3) to determine the physical and chemical properties of the mud mound as far as possible; (4) to infer if the structure is currently active and, if so, how; and (5) to compare the Milano structure with the apparently more active Napoli structure drilled at Site 971.

GEOLOGICAL SETTING

The Milano mud structure forms part of the Olimpi mud dome field (Fig. 2). As summarized in the "Tectonic Introduction" chapter (this volume), the known mud dome fields are located on the northern

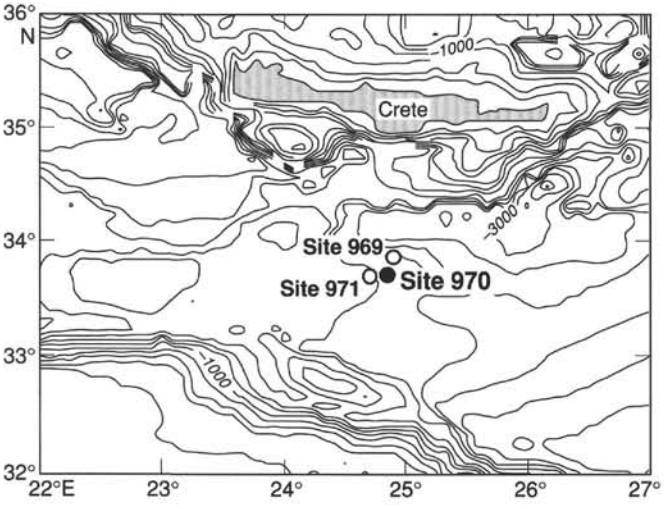

Figure 1. Outline map showing the location of Site 970 at the Milano mud mound.

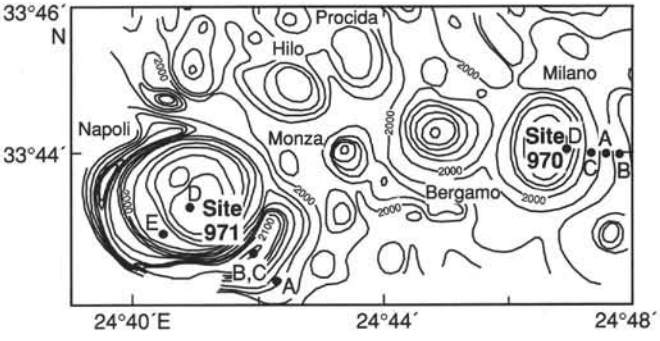

Figure 2. Bathymetric map of the Olimpi mud dome field with the location of cores taken during *Bannock* cruise 89. After Cita and Camerlenghi (1990). Note the locations of the Milano and Napoli mud domes that were cored at Site 970 and Site 971, respectively.

part of the Mediterranean Ridge, along the Inner Escarpment at the northern edge of a wide crestal area, located adjacent to the Inner Plateau. The Inner Plateau to the north is thought to result from flexural loading in response to thrusting of the Mediterranean Ridge accretionary wedge northward, against a backstop including the Hellenic Trench and Crete (Camerlenghi et al., 1995). The Olimpi mud dome field is one of four sited along strike in this general setting.

The Milano structure is one of the smaller features located in the eastern part of the field (Fig. 2). Single-channel seismic reflection reveals an internally structureless conical feature, with more gently sloping flanks that overstep inferred Pliocene-Pleistocene sediments (Fig. 3). The Pliocene-Pleistocene upper surface dips inward such that the mud structure tapers downward to form a central conduit-like structure. The lower flanks are underlain by a moatlike structure, which was imaged during the seismic survey for Site 970 (see "Site Geophysics" section, this chapter). The peripheral flanks are draped with a thin layer of hemipelagic sediments.

Similar mud dome-like structures are known elsewhere within accretionary wedge settings (e.g., Barbados) and have been classified into mud diapirs, mud volcanoes, and mud ridges. Camerlenghi et al. (1995) considered that only one true mud volcano, the Napoli Dome (Site 971), could be recognized in the Olimpi mud dome field, and that the other structures are mud cones and mud ridges. These authors considered the other structures "remnant diapirs," 1–3 km wide, "composed of cone-shaped oval or subcircular mounds below which a conduit is imaged on seismic lines." The ringed seafloor depressions were interpreted in terms of concentric seafloor collapse around each diapiric structure. Similar patterns comprising concentric normal faults have been recognized around a mud eruption cone in the Gulf of Mexico (Prior et al., 1989), and similar features also characterize the mud volcanoes of the Barbados Ridge (Westbrook and Smith, 1983; Brown and Westbrook, 1988; Henry et al., 1990). Possible explanations for the apparent collapse structure are the effects of degassing during the initial stages of mud volcanism and/or dissolution of halite in the Messinian evaporite sequence. The previously available evidence suggested that these moatlike depressions were progressively infilled with mud extrusions and reworked material.

Camerlenghi et al. (1995) envisaged that the mud domes form in stages. During stage 1, gas-rich mud erupts to the surface, accompanied by collapse resulting from degassing, to produce a circular depression infilled with mud. During stage 2, liquid mud extrusions infill the depression and interfinger with the adjacent host sediments. The Napoli mud volcano is believed to represent this stage. Then, during the final stage 3, viscous mud intrudes the conduit and causes final uplift of the surrounding sediments to form a cone-shaped mud dome, including the Milano structure.

In the above model, mud flows fill circular depressions, whereas the cone-shaped structures relate only to late-stage en masse uplift. A different interpretation was suggested by study of high-resolution side-scan sonar records collected during the 1993 cruise of *Gelendzhik* (Limonov et al., 1994). Radiating features were interpreted as mud flows emanating from central vents. If correct, this implies that much of the conical structure of the mud mounds could be built up by the eruption of debris flows, rather than by diapiric uplift. How could these alternatives be distinguished by drilling? In the depression-infilling model, "liquid mud extrusions" would fill a preexisting depression, similar to the infilling of pit craters in volcanoes. In this situation, any clasts carried up by the liquid mud would have an opportunity to settle to form well-defined layers, separated by other layers of mud. On the other hand, in the volcanic extrusion hypothesis, the flows would migrate laterally as true debris flows, in which most of the shear is taken up at bounding shear surfaces, while the interiors of flows would remain as relatively rigid plugs and exhibit a matrix-supported texture. Thus, drilling potentially could distinguish different sediment fabrics and help to test alternative models of mud diapir vs. mud volcano origin, which we hope will lead to the development of a new, more complete interpretation.

OPERATIONS

Transit to Site 970

A 36-nmi seismic survey was run over Sites 970 and 971 (proposed Site MV-2 and proposed Sites MV-1/1 and MV-1/2, respectively) in 6.8 hr at 5.3 kt. A Datasonics 354M beacon (S/N 799, 15.0 kHz) was deployed on the lower flank of Site 970 at 0639 hr on 17 April.

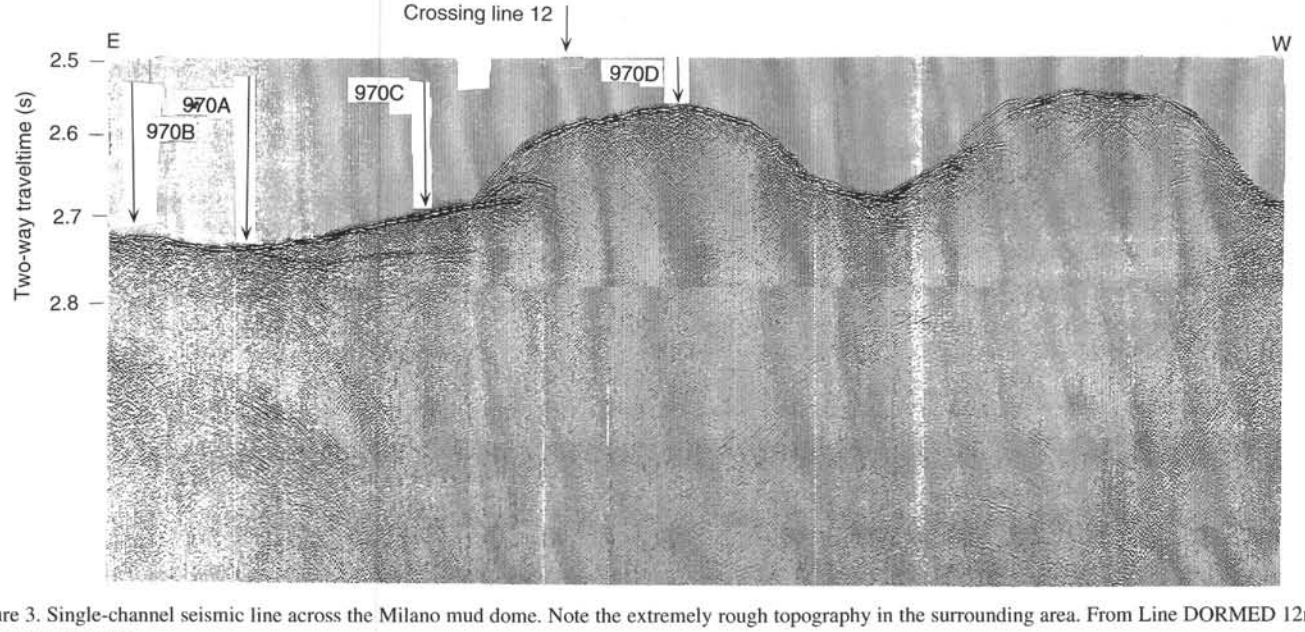

Figure 3. Single-channel seismic line across the Milano mud dome. Note the extremely rough topography in the surrounding area. From Line DORMED 12m, *Bannock* cruise 89 a.

Hole 970A

Hole 970A was spudded at 1120 hr on 17 April on the lower slope of the Milano mud volcano. A seafloor depth of 2075.5 m by drill-pipe measurement (DPM) was indicated. APC Cores 160-970A-1H and 2H were taken from 0 to 10.2 mbsf (Table 1), with 10.2 m cored and 10.24 m recovered (100.4% recovery). Core 160-970A-1H had 30,000-lb overpull off bottom (i.e., the core barrel did not penetrate fully), and Core 2H was rejected with a partial stroke and no overpull in stiff clay with rock debris; therefore, the XCB coring system was deployed. XCB Cores 160-970A-3X through 22X were taken from 10.2 to 201.4 mbsf, with 191.2 m cored and 40.28 m recovered (21.1% recovery). XCB recovery was reduced by sporadic large angular pebbles in hard clay that jammed in the shoe using a short hard-formation shoe and 8- and 9-finger core catchers. Nine of the first 11 XCB cores jammed in the shoe.

A short trip was made to condition the hole for logs, with no drag and 12 m of light fill on the bottom. The hole was displaced with 150 bbl of 8.9-ppg sepiolite/seawater mud and the go-devil was dropped. The pipe was pulled back to 88.8 mbsf for logging. The induction/sonic log was run to total depth (TD) at 2288.4 m below rig floor (mbrf) in 3.08 hr. The density/neutron was run to 2288 mbrf TD in 2.67 hr. The FMS log was run to 2288 mbrf TD in 2.33 hr. Logging finished at 0900 hr on 19 April. The bit cleared the seafloor at 0920 hr on 19 April.

Hole 970B

The ship was moved 800 m east to the distal edge of the Milano mud volcano, and a beacon was dropped at 1021 hr on 19 April. Hole 970B was spudded at 1425 hr on 19 April. The estimated seafloor depth was 2078.6 m DPM. Core 160-970A-1H was probably taken slightly below the seafloor. APC Cores 160-970B-1H through 5H were taken from 0 to 47.5 mbsf (Table 1), with 47.5 m cored and 48.68 m recovered (102.5% recovery). Nannofossil ooze was recovered; therefore, the hole was terminated. The bit cleared the seafloor at 1920 hr on 19 April. The beacon was recovered.

Hole 970C

The ship was moved 1013 m west to the upper flank of the Milano mud volcano, and a Datasonics 354M beacon (S/N 779, 15.0 kHz) was dropped at 2059 hr on 19 April. Hole 970C was spudded at 2300 hr on 19 April. The estimated seafloor depth was 2036.9 m DPM. APC Cores 160-970C-1H through 3H were taken from 0 to 16.5 mbsf (Table 1), with 16.5 m cored and 16.54 m recovered (102.2% recovery). Core 160-970-1H was a partial stroke, which was caused by hitting a siltstone cobble. The maximum headspace gas recorded was 4915 ppm Cl and 3 ppm H_2S.

XCB Cores 160-970C-4X and 5X were taken from 16.5 to 35.6 mbsf, with 19.1 m cored and 0.43 m recovered (2.3% recovery). XCB recovery was reduced by sporadic large angular pebbles in hard clay that lodged in the shoe acting as a center bit. The bit cleared the seafloor at 0350 hr on 20 April. The beacon was recovered.

Hole 970D

The ship was moved 720 m west to the crest of the Milano mud volcano, and a Datasonics 354M beacon (S/N 1243, 14.0 kHz) was dropped at 0448 hr on 20 April. Hole 970D was spudded at 0715 hr on 20 April. The estimated seafloor was at 1953.3 m DPM. APC Cores 160-970D-1H through 5H were taken from 0 to 42.8 mbsf (Table 1), with 42.8 m cored and 44.19 m recovered (103.2% recovery). The last four cores were partial strokes in hard clay with pebbles and gravel, and Core 160-970D-2H had a split liner. The bit cleared the seafloor at 1010 hr on 20 April. The beacon was recovered and the transit to Site 971 began.

Table 1. Coring summary for Site 970.

Core	Date (April 1995)	Time (UTC)	Depth (mbsf)	Length cored (m)	Length recovered (m)	Recovery (%)
160-970A-						
1H	17	0930	0.0–7.6	7.6	7.63	100.0
2H	17	1015	7.6–10.2	2.6	2.61	100.0
3X	17	1145	10.2–18.2	8.0	0.45	5.6
4X	17	1330	18.2–27.8	9.6	1.54	16.0
5X	17	1440	27.8–37.4	9.6	0.21	2.2
6X	17	1550	37.4–47.1	9.7	0.70	7.2
7X	17	1640	47.1–56.7	9.6	0.59	6.1
8X	17	1755	56.7–66.3	9.6	0.39	4.1
9X	17	1910	66.3–76.0	9.7	0.67	6.9
10X	17	2105	76.0–85.7	9.7	0.90	9.3
11X	17	2230	85.7–95.4	9.7	0.50	5.2
12X	17	2345	95.4–105.1	9.7	0.25	2.6
13X	18	0115	105.1–114.8	9.7	0.68	7.0
14X	18	0300	114.8–124.4	9.6	0.60	6.3
15X	18	0445	124.4–134.0	9.6	3.45	35.9
16X	18	0555	134.0–143.6	9.6	3.74	38.9
17X	18	0700	143.6–153.2	9.6	5.61	58.4
18X	18	0825	153.2–162.8	9.6	4.41	45.9
19X	18	0950	162.8–172.5	9.7	4.20	43.3
20X	18	1130	172.5–182.1	9.6	2.47	25.7
21X	18	1335	182.1–191.7	9.6	3.35	34.9
22X	18	1530	191.7–201.4	9.7	5.52	56.9
Coring totals:				201.4	50.5	25.1
160-970B-						
1H	19	1305	0.0–9.5	9.5	9.72	102.0
2H	19	1350	9.5–19.0	9.5	9.75	102.0
3H	19	1455	19.0–28.5	9.5	9.95	105.0
4H	19	1530	28.5–38.0	9.5	9.96	105.0
5H	19	1640	38.0–47.5	9.5	9.30	97.9
Coring totals:				47.5	48.7	102.5
160-970C-						
1H	19	2115	0.0–5.2	5.2	5.20	100.0
2H	19	2205	5.2–8.2	3.0	3.02	100.0
3H	19	2250	8.2–16.5	8.3	8.32	100.0
4X	20	0025	16.5–26.0	9.5	0.38	4.0
5X	20	0125	26.0–35.6	9.6	0.05	0.5
Coring totals:				35.6	17.0	47.7
160-970D-						
1H	20	0525	0.0–4.8	4.8	4.79	99.8
2H	20	0605	4.8–14.3	9.5	10.02	105.5
3H	20	0640	14.3–23.8	9.5	10.20	107.3
4H	20	0705	23.8–33.3	9.5	9.22	97.0
5H	20	0740	33.3–42.8	9.5	9.96	105.0
Coring totals:				42.8	44.2	103.2

SITE GEOPHYSICS

Two mud domes were chosen for drilling: Napoli and Milano. These two mud structures differ in appearance and composition. Milano is a sonar-bright dome in the shape of a wide-brimmed mexican hat and Napoli is a dome of low reflectivity in the form of a derby. Previous sampling had shown that the surface of Milano is formed by layers, possibly flows, of a so-called mud breccia made up of clasts in a mud matrix (see "Geological Setting" section, this chapter). The clasts in the breccia form a "volume scatterer" of sonar and seismic energy, which causes poor seismic penetration and the sonar-bright surface appearance in side-scan images (Volgin and Woodside, in press).

The predrilling survey for Site 970 was made up of two passes across Milano (Fig. 4). One east-northeast to west-southwest line followed a previous *Bannock* line but displayed a great deal more subsurface information; the second line crossed the feature obliquely from southwest to northeast. The seafloor is smoother over the mud volcano than over the adjacent seafloor, probably because the mud flows smooth out the small-scale relief. The character of the 3.5-kHz signal over the mud dome changes abruptly at the outer edge of the inferred mud flows: over the mud volcano the seafloor echo is not much stronger than the general reverberation that is received later, but over the neighboring seafloor the bottom gives a strong peak and the signal drops off fairly quickly thereafter.

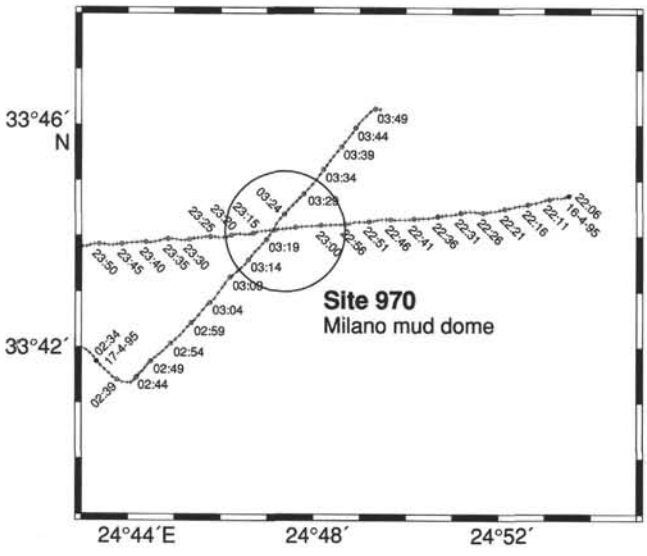

Figure 4. Track chart showing the predrilling site-survey lines across the Milano mud volcano at Site 970.

The seismic profiles (Fig. 5) indicate a very asymmetric subsurface structure to the mud volcano. Reflectors generally dip inward toward mud volcanoes; this has been inferred to result from collapse of the surrounding strata, but also results in part because of diffractions from point reflectors around the central conduit. Velocity pull-down below Milano is unlikely to be a significant cause of inward-dipping reflectors because the seismic velocity of mud breccia is most likely higher rather than lower than the surrounding near-surface sediments. The inward-dipping reflectors below Milano are displaced toward the east, indicating that the central core of the structure is about 1 km east of the geometric center of the topographic dome.

Several strong reflectors are seen below Milano, possibly as a fortuitous result of the long signal length and low frequency of the seismic system used on *JOIDES Resolution*. One strong reflector marking the base of the accumulated sediment beneath the mud dome, at a total depth of about 3.4 s two-way traveltime (TWT), slopes upward toward the upper flanks of the dome, like a deep crater containing the mud breccia above. Another strong reflector dips eastward, from the lowest point of the basement reflector beneath the dome, extending from a depth of 3.6 s TWT to a depth of more than 3.9 s TWT beneath the outer eastern flanks. A third strong reflector lies directly below the thickest part of the mud dome at a depth of 3.85 s TWT, resembling the magma chamber beneath an igneous volcano but here representing the downfaulted continuation of the eastward-dipping reflector beneath the mud volcano. No reflectors appeared to show phase reversals that might have indicated zones of overpressured fluids and gases beneath the mud volcano as the source of the strong reflections. Likewise, no bottom-simulating reflectors were observed that might have suggested the presence of gas hydrates. These deeper structures have not been seen in previous data obtained from the Olimpi Field.

The drilling sites were chosen across the eastern flank of the mud dome from the crest to beyond the last shallow appearance of the mud breccias inferred to form the slope of the mud volcano at depths of less than 1 to 2 m (Volgin and Woodside, in press). Below the flank, upward- and eastward-sloping reflectors that appear to pinch out near the apparent edge of the inferred mud flows can be discerned. These reflectors are interpreted to result from interfaces between several large mud eruptions from a central source. Because it was desired to penetrate several flows and possible interbedded pelagic sediments, the site-survey information was used to find a location where the units defined by these reflectors thin toward a pinch out. Two other sites were located on the flank of the mud volcano where mud flows could be inferred from the seismic and 3.5-kHz data; and a location on the geometric center of the crestal part of the mud dome was found for the last hole.

LITHOSTRATIGRAPHY

Four holes on a transect from the base to the crest of the Milano mud volcano were cored at Site 970 (Fig. 6). Two lithostratigraphic units were identified on the basis of visual observation of color, sedimentary structure, smear-slide composition, bulk mineralogy by X-ray diffraction (XRD), and carbonate determination. A lithostratigraphic summary of Site 970 is shown in Figure 7.

Unit I consists of light-colored intervals of nannofossil clay and nannofossil ooze, with minor clayey nannofossil ooze, together with distinct dark-colored sapropels, which are composed of clay, nannofossil clay, and clay with nannofossils and foraminifers. All of these beds are enriched in organic carbon and contain disseminated organic matter and pyrite, with variable amounts of quartz, inorganic calcite, and plant fragments. Volcanic glass is rare.

Unit II consists mainly of a matrix of dark greenish-gray mud with nannofossils, clay, foraminifers, quartz, and rock fragments, together with abundant, heterogenous clasts that vary in size. The textures observed allow a threefold division of Unit II to be made:

Subunit IIA, matrix-supported clast-rich debris-flow deposits: dark gray silt- to medium-sand-grade matrix with variable quantities of rounded to angular clasts varying in size from a few millimeters to tens of centimeters suspended within it with no obvious sorting. Some vesicular structure was found.

Subunit IIB, matrix-supported breccia/conglomerate: dark gray mud- to silt-grade matrix supporting both variable abundances of centimeter- to decimeter-size clasts and abundant clasts approximately 1 cm in diameter.

Subunit IIC, polymictic gravel: multiple intervals of gravel- or microconglomerate-grade clasts fining upward to silt- or clay-grade dark gray material.

Description of Lithostratigraphic Units

Lithostratigraphic Unit I

Description: Nannofossil clay, nannofossil ooze, and clayey nannofossil ooze
Intervals: Sections 160-970A-1H-1, 0–60 cm, 4X-1, 53 cm, through 4X-CC, 16X-1 through 18X-1, 28 cm, 22X-1, 60 cm, through 22X-CC, and Cores 160-970B-1H through 5H
Depth: 0–0.6, 18.73–19.74, 134.0–153.47, and 192.3–201.4 mbsf, Hole 970A; 0–47.5 mbsf, Hole 970B
Age: late Pliocene to late Pleistocene

The lithology of Unit I is dominated by alternations of light grayish brown (10YR 5/2), light gray (10Y 6/1), gray (10Y 4/1), and greenish gray (5GY 5/1) nannofossil clay, nannofossil ooze, and clayey nannofossil ooze. Smear-slide analyses indicate that the sediment is composed of between 5% and 75% clay and between 20% and 80% nannofossils (Fig. 8). Carbonate content fluctuates between 4% and 68%, and organic carbon values are between 0.1% and 0.5% (see "Organic Geochemistry" section, this chapter). Minor components include quartz, volcanic glass, and inorganic calcite. Sapropels are between 1 and 30 cm thick, and consist of dark gray (5Y 4/1), very dark gray (5Y 3/1), and black (5Y 2.5/1) clay, and clay with nannofossils and foraminifers. Minor components include disseminated amorphous organic matter, usually with pyrite, together with variable admixtures of quartz, inorganic calcite, and plant fragments. Volcanic glass is rare.

Lithostratigraphic Unit II

Description: Matrix-supported clast-rich debris-flow deposits, matrix-supported breccia/conglomerate, and polymictic gravel

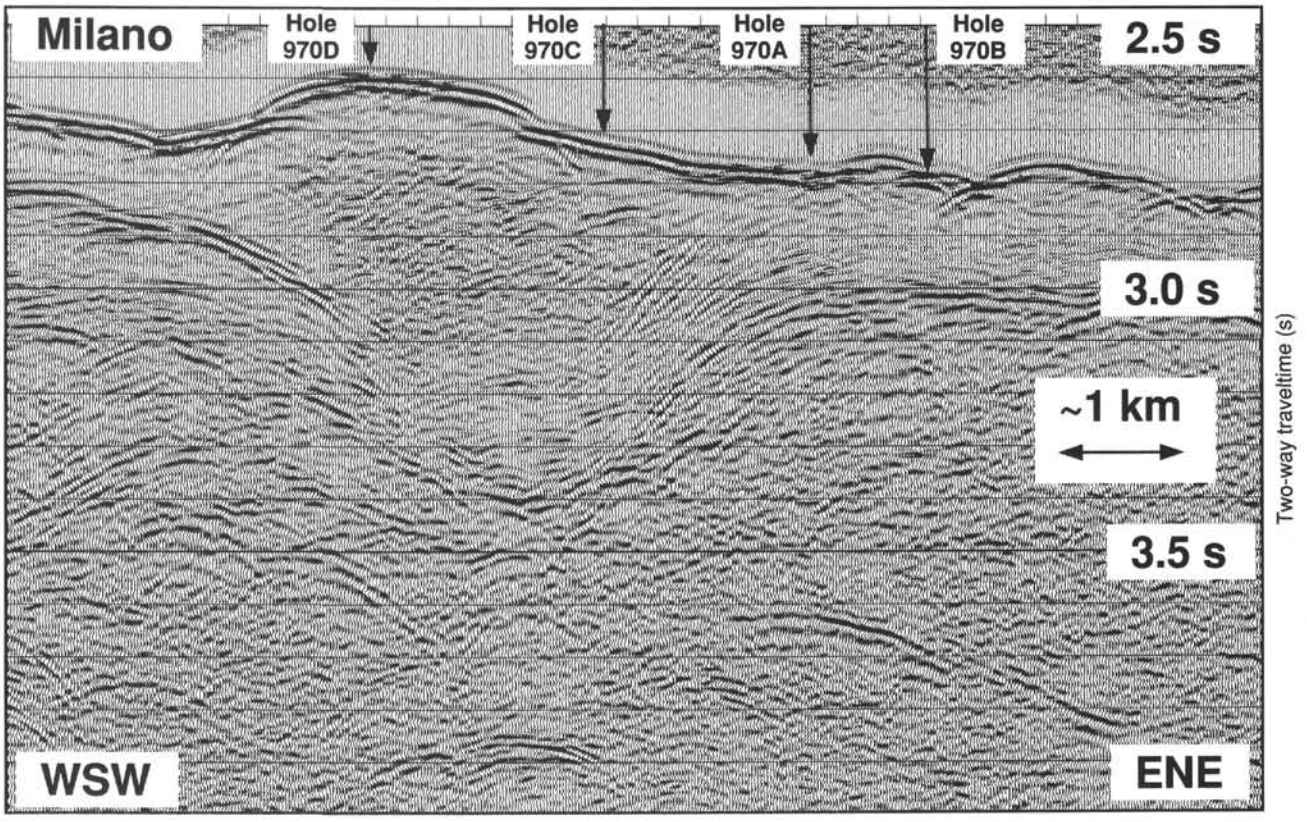

Figure 5. Seismic profile across the Site 970 transect, Milano mud dome.

Intervals: Sections 160-970A-1H-1, 60 cm, through 4X-1, 45 cm, 5X-1 through 15X-3, 45 cm, and Cores 160-970A-18X through 21X, 160-970C-1H through 5X, and 160-970D-1H through 5H
Depth: 0.6–18.73, 19.74–134.0, 153.47–192.3 mbsf, Hole 970A; 0–26 mbsf, Hole 970C; 0–42.8 mbsf, Hole 970D
Age: Pleistocene

Lithostratigraphic Subunit IIA

Description: Matrix-supported clast-rich debris-flow deposits
Intervals: Sections 160-970A-1H-1, 60 cm, through 1H-CC, 160-970C-1H-1 through 4X-1, and 160-970D-1H-1 through 5H-CC
Depth: 0.6–7.60 mbsf, Hole 970A; 0–16.90 mbsf, Hole 970C; 0–42.80 mbsf, Hole 970D
Age: Pleistocene

The sediment in Subunit IIA consists of a dark gray, dominantly silty to clayey matrix with clasts of variable lithology, size, and shape. Smear-slide analyses show that the principal components of the matrix are nannofossils, foraminifers, clay, quartz, and rock fragments (Fig. 8). The carbonate content values for this subunit are in general much lower than those for Unit I, varying from 10.1% to 24.0% (see "Organic Geochemistry" section, this chapter).

Variation in the grain size of the matrix is evident in both Holes 970D and 970C. In Hole 970D, for instance, the upper two cores consist of silt-clay grade material, whereas Cores 160-970D-3H through 5H have a fine- to medium-sand-grade matrix. A similar but smaller scale variation was seen in Hole 970C. The maximum clast size recovered per meter in Subunit IIA is plotted against depth in Figure 9 for Holes 970A, 970C, and 970D. With the exception of a few outsized clasts, the maximum clast size within this subunit is consistent in all holes, varying between 1 and 5 cm. It is possible that this is an artifact of drilling, but given the good recovery (Fig. 7) this distribution is thought to reflect the approximate grain-size population for Subunit IIA.

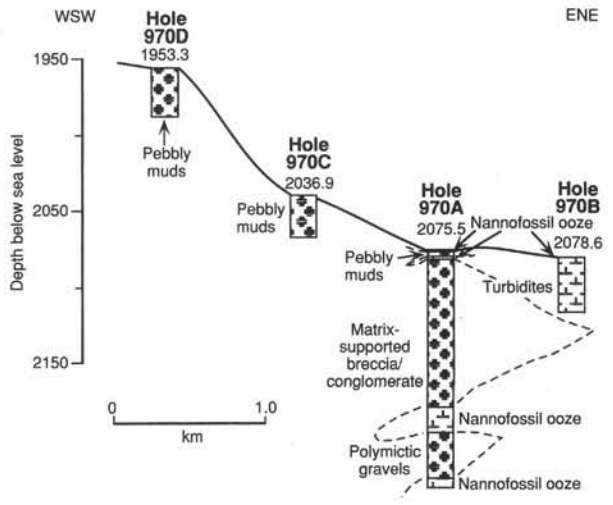

Figure 6. A cross section along the transect of holes drilled at Site 970. The dashed line represents a schematic interpretation of the interfingering relationship of the hemipelagic (Unit I) and mud breccia (Unit II) sediments.

Estimations of the clast:matrix ratio suggest that clast abundance decreases toward the bottom of the section in Hole 970D (i.e., 15%–40% on average, but 5%–10% for the basal sections of Core 160-970D-5H). In Holes 970A and 970C, the abundance of clasts ranges from 10% to 20% without any obvious systematic variation.

Many of the cores in Holes 970C and 970D contain abundant small gas vesicles (e.g., Cores 160-970C-1H through 3H and 160-970D-1H and 2H), which give the appearance of frothy mousselike

texture. This texture is apparent only in the finer grained sediments. In previous studies on comparable material, this texture was also described as mousselike (e.g., Camerlenghi et al., 1992; Staffini et al., 1993) and was thought to be caused by the presence of solid-state gas hydrates in the sediment prior to drilling (e.g., Westbrook, Carson, Musgrave, et al., 1994). The upper core from both Holes 970C and 970D contained a large amount of methane (see "Organic Geochemistry" section, this chapter).

In neither Hole 970C nor 970D was the base of the matrix-supported clast-rich debris-flow deposits penetrated. The upper contact of this subunit in both these holes is the sediment/water interface. In Hole 970A, however, Subunit IIA is overlain by a thin (40 cm thick) section of Unit I with a gradational contact (Table 2) and underlain by Subunit IIB. The contact between these two mud breccia subunits was not recovered.

Lithostratigraphic Subunit IIB

Description: Matrix-supported breccia/conglomerate
Interval: Sections 160-970A-2H-1 through 15X-3
Depth: 7.60–18.73 and 19.74–134.0 mbsf
Age: middle to late Pleistocene

The recovery of this subunit was generally low (2%–35%, with the exception of Core 160-970A-2H; Fig. 7), which made detailed description of fabrics common to the entire interval impossible. Textural characteristics of the material recovered, however, suggest that Subunit IIB consists of silt- to gravel-sized clasts supported in a matrix of dark gray nannofossil mud that contains abundant mica flakes and pyrite (Fig. 10). Smear-slide analyses indicate that the principal components of the matrix are nannofossils, foraminifers, clay, quartz, and rock fragments (Fig. 8). The carbonate content and organic carbon values for this subunit are in general much lower than those for Unit I, varying from 8.8% to 18.6% and 0% to 0.82%, respectively (see "Organic Geochemistry" section, this chapter). Higher values were found within the matrix-supported breccia/conglomerates, but they correspond either to an interval of Unit I (Sections 160-970A-4X-1 and 4X-CC) or to a sample taken from a large mud clast (Fig. 30, "Organic Geochemistry" section, this chapter).

No clasts greater than 2 cm in diameter were observed in Cores 160-970A-2H and 3X. Core 160-970A-4X comprises the interval of Unit I mentioned above. This may represent either in situ material interbedded with the mud breccias or a displaced rafted clast of hemipelagic sediment caught up within the mud breccias. In Cores 160-970A-5X through 15X, larger clasts (up to 135 mm in diameter; Fig. 11) were recovered. These clasts are supported by material similar to that found in Cores 160-970A-2H and 3X (Fig. 10), which results in the appearance of two distinct grain-size populations supported by a finer grained matrix. The variation of clast size (where clasts can be unambiguously identified) with depth is tentatively presented in Figure 11.

Lithostratigraphic Subunit IIC

Description: Polymictic gravel
Interval: Sections 160-970A-18X-1, 28 cm, through 22X-1, 60 cm
Depth: 153.47–192.3 mbsf
Age: early Pleistocene to late Pliocene

Subunit IIC consists of centimeter- to decimeter-thick graded sequences (Fig. 12) interbedded with subordinate alternations of gravel-, sand-, and mud-grade material, where no grading was observed. The basal layers of the graded sequences contain angular to rounded clasts, up to 2 cm in diameter, that are clast supported and generally fine upward through sand-grade material to silt and nannofossil clay. Reverse grading at the base of a larger fining-upward unit was observed in Section 160-970A-19X-2, 80–90 cm. The nongraded units are both clast and matrix supported in places. In some cases, well-sorted layers with sharp boundaries are interbedded. Less well-sorted layers (Section 160-970A-19X-2, 0–25 cm) were also seen. Rare, darker organic-rich layers interbedded with millimeter-scale graded lamination were seen in Section 160-970A-18X-2, 104–107 cm (Fig. 13). Smear-slide analysis suggests that the composition of the finer material is heterogeneous and consists of varying abundances of nannofossils, foraminifers, clay, quartz, and rock fragments (Fig. 8). Carbonate content and organic carbon values for this interval are low, ranging between 17.5% and 29.8% and 0.05% and 0.6%, respectively (see "Organic Geochemistry" section, this chapter). Small euhedral pyrite grains can be seen throughout the sequence.

Clast Descriptions

Most of the clast types found in the mud breccias are common to all three subunits recovered at Site 970. Clast lithologies fall into four main groups: mudstones, sandstone, siltstone, and foraminiferal micritic rocks. The composition, angularity, and maximum size of the clasts observed are listed in Table 3. The observation of both angular and rounded clasts of all lithologies suggests that the relationship between clast lithology and angularity is not simple. Early to middle Miocene (Burdigalian-Langhian) material appears to dominate clast age (see "Biostratigraphy" section, this chapter).

The sandstones contain a mixed grain population (Table 3) indicating grain derivation from multiple sources including metamorphic rocks (micaceous schists, metacarbonates, microcline, quartz with well-developed subgrains), plutonic igneous rocks (quartz with fluid inclusions), and sediments (glauconite, echinoid spines, foraminifers, well-rounded grains; Fig. 14). Faunal evidence from some of the mud clasts also suggests that reworking of Oligocene, Eocene, and Cretaceous material occurred during the early Miocene ("Biostratigraphy" section, this chapter). Planktonic foraminiferal micrite clasts of early Miocene age suggest relatively deep-water accumulation at this time (see "Biostratigraphy" section, this chapter). One clast of cross-laminated siltstone is in contact with the lower to middle Miocene micrites (Fig. 15) suggesting that some of, if not all, the different clast types could have come from a lower Miocene interval.

Matrix

Initial description indicates that the matrix composition varies both within and among the subunits at Site 970. Smear-slide analyses suggest that the matrix is composed of components similar to Unit I, but in differing abundances. Nannofossils and foraminifers are far less abundant in the mud breccias than in Unit I, whereas clay, quartz, and rock fragments are more common. Both the carbonate content and organic carbon values are lower for Unit II than Unit I (see "Organic Geochemistry" section, this chapter).

Structural Information

Measurement of structures was conducted only on the pelagic sedimentary sequences of Unit I; the data are listed in Table 4. Almost all the bedding and fault information was obtained from Hole 970B, where the bedded nature of the sediment and the APC coring technique used allowed measurement of both bedding planes and faults relative to the core coordinate system. In Cores 160-970B-2H, 4H, and 5H, tilted beds are common.

Tensor data were available only for Cores 160-970B-3H through 5H. Corrected structural measurements with respect to geographic coordinates for this interval indicate no systematic dip directions (cf., Table 3), with slight to moderate tilting of the planes (5°–15°).

The irregular sedimentary contacts found at several intervals (e.g., Sections 160-970B-2H-6 through 2H-7 and 4H-1) are thought to be the result of slight scour on the base of debris flows. Mud clasts up to 8 cm in diameter (e.g., Section 160-970B-2H-7) can be identified in the cores, but the presence of larger clasts that either were the cause

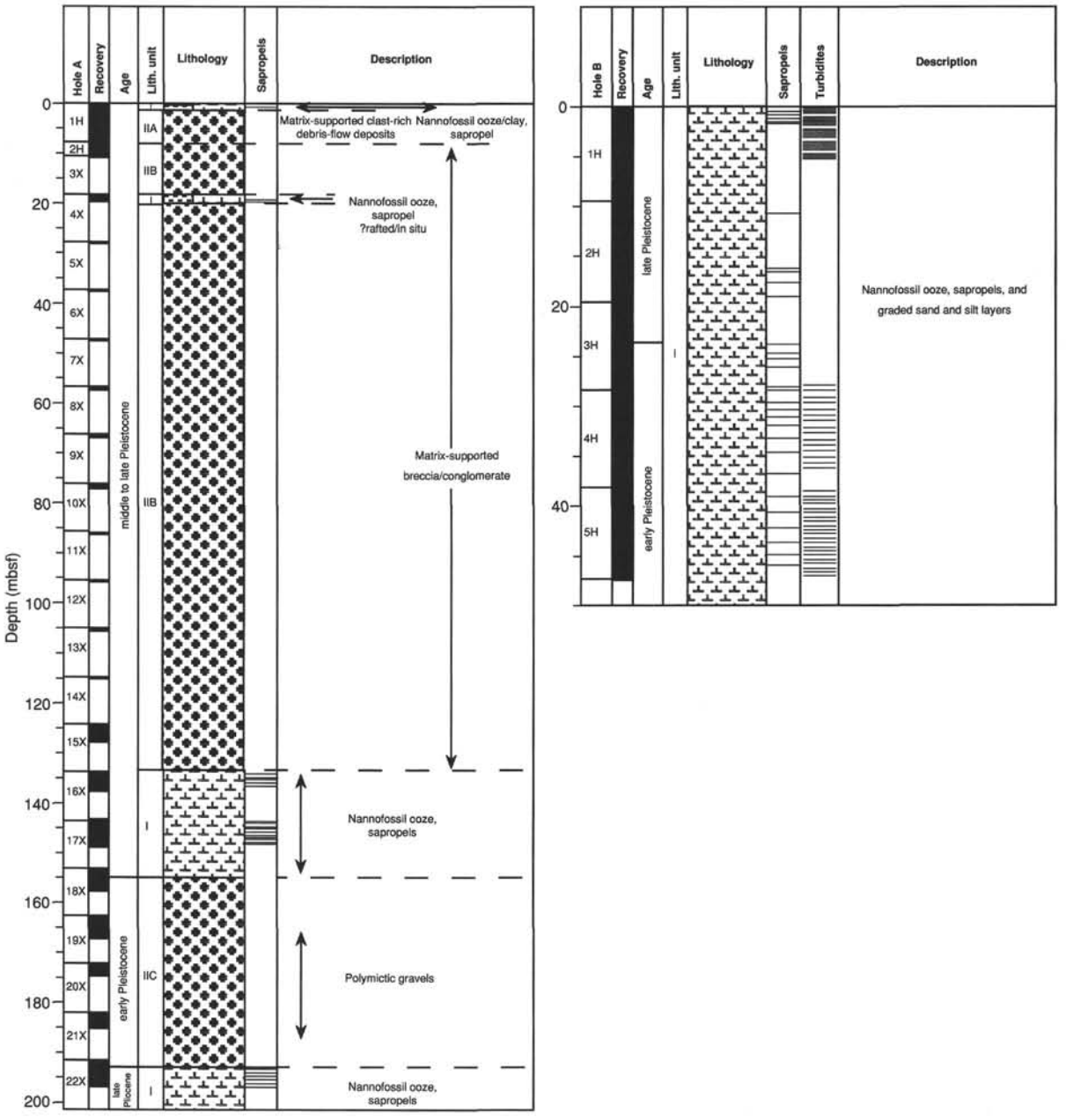

Figure 7. Core recovery, age information, lithostratigraphic summary, and age information for Site 970.

of poor recovery or were misidentified as in situ material cannot be excluded from core-scale observations.

Microfaulting is concentrated in Sections 160-970B-5H-2 through 5H-4, where both normal and reverse faults, with offsets of 0.5 cm to more than 6 cm, disrupt the layered succession. Most of the normal faults dip steeply (60°–75°) toward either the northwest or southeast.

Interpretation

Detailed shore-based sedimentological and paleontological study is required to substantiate the initial results obtained at Site 970. However, a few general points can be made that permit an initial interpretation of deposition of the Milano mud volcano sediments: (1) the mud breccias interfinger with the hemipelagic sediment in Hole 970A (Fig. 6), (2) mud breccia was not recovered in Hole 970B, (3) multiple graded sand and silt layers in Hole 970B are of equivalent age to the mud breccia units in Hole 970A, (4) a period of hemipelagic sedimentation occurred in the late early Pleistocene in Holes 970A and 970B, (5) there is clear evidence for multiple flows in the polymictic conglomerate recovered in the lower part of Hole 970A, and (6) a similar range of heterogenous clast types was found throughout the mud breccia unit.

Mechanisms of Mud Volcano Deposition

Previous investigation of the Mediterranean Ridge mud volcanos was based upon seismic and piston core data (e.g., Cita et al., 1981, 1994; Camerlenghi et al., 1992; Staffini et al., 1993). From this information a number of hypotheses have been put forward. These fall into

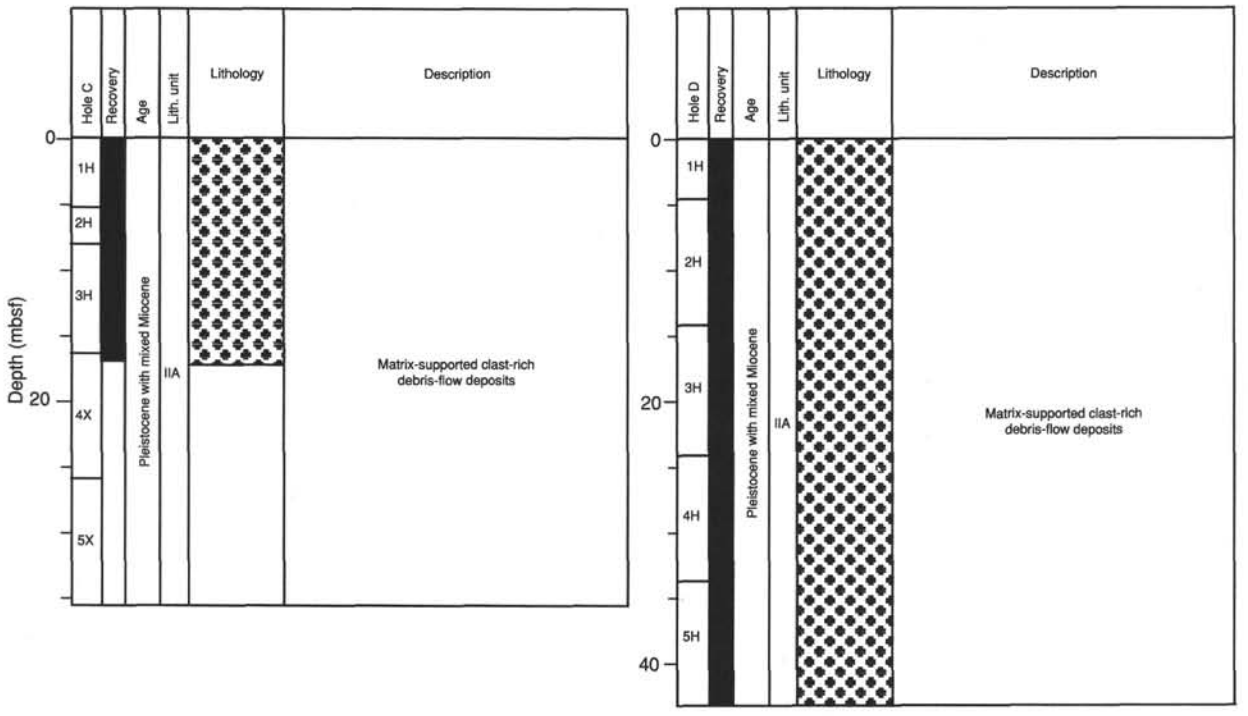

Figure 7 (continued).

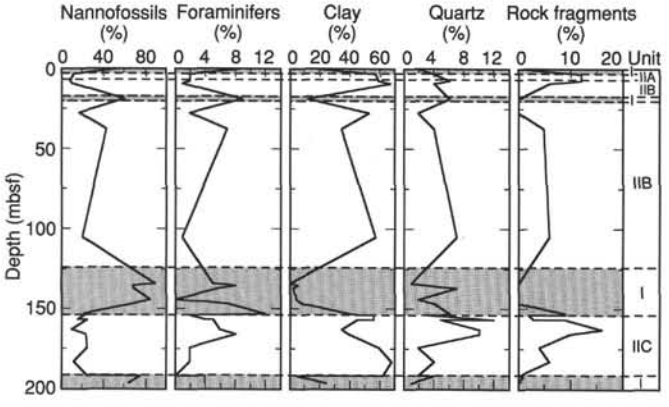

Figure 8. Smear-slide data for selected sedimentary components at Site 970. Shaded areas indicate intervals of pelagic sediments.

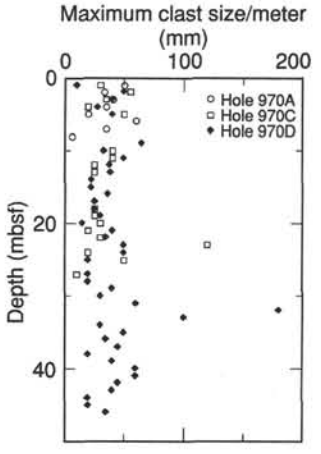

Figure 9. Maximum clast size per meter plotted against depth for Subunit IIA (matrix-supported clast-rich debris-flow deposits) in Holes 970A, 970C, and 970D.

two general categories, one related to diapiric intrusion, the other to extrusive flow (Cita et al., 1981; Camerlenghi et al., 1992).

The most convincing evidence for extrusion and flow rather than deposition as in situ diapirs is the interbedding of hemipelagic sediments and mud breccias, as seen in Hole 970A. Evidence for both debris-flow and turbidity current deposition is present in the lower Pleistocene deposits. The grading and sorting observed in the polymictic gravels (Subunit IIC) are probably indicative of turbidity flow, with the possibility that some of the coarser beds were deposited by debris-flow mechanisms (e.g., reverse grading as a result of traction carpet formation and frictional freezing; Lowe, 1982). The spatial geometry of the mud breccia and hemipelagic deposits along the transect (Fig. 6) indicates that there is an interfingering relationship that is far more likely the result of extrusive sedimentation than diapiric intrusion.

There appear to have been two periods of active clastic sedimentation in Holes 970A and 970B, separated by a time during which hemipelagic sediments accumulated. One possible interpretation is that this period of hemipelagic sedimentation represents a time when the Milano volcano was relatively quiescent. Another alternative, given that only one flank of the volcano was cored at Site 970, is that asymmetrical extrusion and channeling of material elsewhere on the cone took place during pelagic deposition on the northeastern flank.

Poor recovery of the matrix-supported breccia/conglomerate makes the identification of individual flow contacts within the subunit, if they exist, extremely difficult to see. The FMS data, however, suggest that there are several changes in the log character of the lower part of this sequence that could indicate lithologic changes (see "Downhole Measurements" section, this chapter). Further study of the clast size and matrix grain size will be required to identify these boundaries in the recovered core.

Table 2. Summary of primary observations of the mud breccia subunits.

	Subunit IIA: matrix-supported clast-rich debris-flow deposits	Subunit IIB: matrix-supported breccia/ conglomerate	Subunit IIC: polymictic gravel
Sorting	Massive	Recovery not sufficient to determine	Normal grading common; reverse grading and chaotic beds rare
Fabric	Matrix-supported	Matrix-supported	Clast-supported with rare matrix-supported fabrics
Matrix	Silt-sand	Silty claystone throughout	?
Grain population	Mixed pebble to silt grade	Three groups: silty clay, 1-cm clasts, and pebbles	Gravel to clay
Angularity	Angular to rounded	Angular to rounded	Subrounded
Gas-derived texture	Mousse fabric	?	?
Upper contact	Gradational in Hole 970A to overlying hemipelagic sediment	Not exposed	Sharp contact with overlying hemipelagic sediment in Section 160-970A-18X-1, 28 cm
Clast size	Up to 120 mm	Up to 140 mm (FMS indicates up to 0.6 m)	Up to 50 mm

BIOSTRATIGRAPHY

Calcareous Nannofossils

Hole 970A

Hole 970A was drilled into the flank of Milano mud volcano. The sediments recovered are primarily mud breccias with some intercalations of pelagic ooze (see "Lithostratigraphy" section, this chapter). Calcareous nannofossils were studied primarily from core-catcher samples. Sixteen additional samples were collected from the matrix and clasts. Owing to considerable reworking and a paucity of nannofossils in most intervals, the biostratigraphy from Hole 970A requires a greater degree of interpretation than usual. Most of the cores recovered are composed of sediments that contain only a sparse, mostly reworked, nannofossil assemblage that could not be dated. Fortunately, these poor-quality samples contain intercalations of pelagic nannofossil oozes composed of excellently preserved assemblages that could be dated.

The ages of well-preserved in situ nannofossils collected from samples of the matrix range from late Pleistocene to late Pliocene. Although many clasts do not contain appreciable nannofossil assemblages, some clasts contain abundant, moderately preserved nannofossils. The ages of the clasts in Hole 970A range from the early to middle Miocene (Burdigalian-Langhian). Some of the clasts contain reworked Late Cretaceous and middle Eocene age assemblages in addition to the Miocene material.

Because all of the nannofossil zones were observed within the pelagic intervals, the sequence recovered at Site 970 is considered to represent continuous pelagic deposition punctuated by rapid deposition of debris-flow deposits that contain abundant clasts of various compositions. This episodic deposition has resulted in a sequence of sediments unsuitable for definitive biostratigraphic interpretations intercalated with thin layers of pelagic sediment of significant biostratigraphic value. A summary of the biostratigraphy is described below and displayed in Figure 16.

Owing to considerable reworking of older taxa and dilution from material derived from the mud volcano, *Emiliania huxleyi* was not observed in the first two core-catcher samples. However, *E. huxleyi* was noted in Sample 160-970A-3X-CC and pelagic Sample 160-970A-4X-1, 110 cm. The presence of *E. huxleyi* in these samples indicates that all sediments above Sample 160-970A-4X-1, 110 cm, were redeposited into Zone MNN21a. The accompanying assemblage includes small *Gephyrocapsa* (<3.5 µm), *Gephyrocapsa oceanica* s.l., *Helicosphaera kamptneri, Coccolithus pelagicus, Rhabdosphaera clavigera,* and *Pontosphaera japonica.* There is little to no reworking evident in the pelagic sample. Specimens of reworked early to middle Miocene age fossils dominate the nonpelagic intervals.

Samples 160-970A-5X-CC through 10X-CC are of poor biostratigraphic value and contain a mixture of nannofossils that range in age from Late Cretaceous to Pliocene. Conversely, Sample 160-970A-11X-CC contains little reworked material and abundant quantities of Pleistocene *G. oceanica* s.l. and small *Gephyrocapsa* without *E. huxleyi* or *Pseudoemiliania lacunosa.* The assemblage indicates that this sample, and maybe the sediments that contained older fossils above, are within Zone MNN20. Samples 160-970A-12X-CC through 14X-CC contain rare to few nannofossils that include *Cyclicocargolithus floridanus, H. kamptneri, Reticulofenestra umbilica,* and *Reticulofenestra* sp. (>7 µm). The assemblage in these samples is not age diagnostic and is probably redeposited from Miocene and Eocene sources.

Beginning in Sample 160-970A-15X-CC a pelagic interval containing abundant nannofossils is present. Sample 160-970A-15X-CC contains an assemblage from Zone MNN19f that includes *P. lacunosa* and *G. oceanica* s.l. *Gephyrocapsa* sp. 3, which occurs in the lower part of Zone MNN19f, is contained in Samples 160-970A-16X-2, 14 cm, and 16X-2, 98 cm. Nannofossils representing Zone MNN19e were found in Samples 160-970A-16X-2, 141 cm, and 16X-3, 24 cm. This zone lacks both large *Gephyrocapsa* (>5.5 µm) and *Helicosphaera sellii.* From Samples 160-970A-16X-CC through 17X-4, 30 cm, large *Gephyrocapsa* (>5.5 µm) and *H. sellii* become a part of the assemblage, which indicates that these samples are within Zone MNN19d.

From Samples 160-970A-18X-CC through 22X-1, 46 cm, gray clast-bearing muds were observed. Most of these intervals contain a nannofossil assemblage dominated by middle Miocene species. This interval of displaced fossils also contains minor amounts of late Pliocene age taxa. The gray muds are bounded by pelagic units from Zones MNN19d and MNN19b, which indicates that the muds were redeposited in the early Pleistocene.

Sample 160-970A-22X-1, 100 cm, was collected from a pelagic interval just below the clast-bearing muds. Nannofossils from this sample include *Calcidiscus macintyrei* and *G. oceanica* s.l., which are representative of Zone MNN19b. Sample 160-970A-22X-2, 98 cm, does not contain *G. oceanica* s.l. and was placed into uppermost Pliocene Zone MNN19a. The last collected Samples 160-970A-22X-3, 86 cm, through 22X-CC contain *Discoaster brouweri* and *Discoaster triradiatus* and were placed into Zone MNN18.

Hole 970B

Hole 970B was drilled on the basin floor adjacent to the Milano mud volcano. Sediments recovered from this site are pelagic ooze and contain nannofossils that range in age from late-middle Pleistocene to early Pleistocene (Fig. 17).

Samples 160-970B-1H-1, 40 cm, through 1H-5, 120 cm, contain an assemblage that includes *G. oceanica* s.l., *Calcidiscus leptoporus,* small *Gephyrocapsa,* and *Syracosphaera pulchra.* All but the first of these samples contain rare quantities of *E. huxleyi.* The presence of *E. huxleyi* in the first sample was probably obscured by abundant clasts and generally poorer preservation than was observed in the samples immediately below.

Samples 160-970B-1H-6, 120 cm, and 1H-CC contain neither *E. huxleyi* nor *P. lacunosa.* Therefore, the samples were placed into Zone MNN20.

Samples 160-970B-2H-CC through 3H-3, 110 cm, contain *P. lacunosa* in an assemblage similar to that of the preceding zone. Samples 160-970B-3H-1 and 3H-3, 110 cm, contain *Gephyrocapsa* sp. 3.

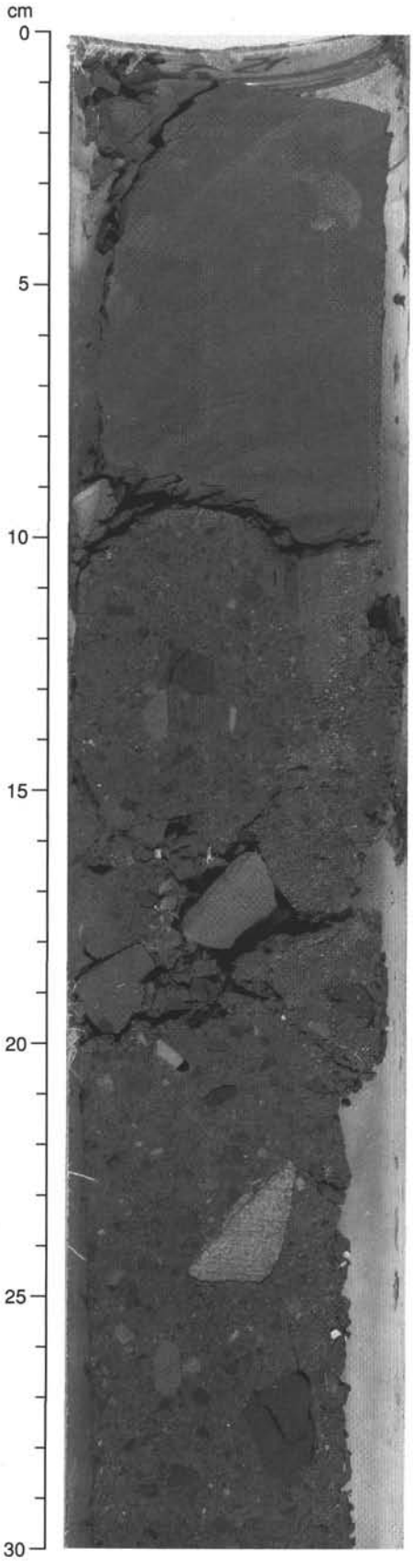

Figure 10. Photograph showing the bimodal grain-size population of the matrix-supported breccia/conglomerate Subunit IIB (Section 160-970A-15X-1, 0–30 cm).

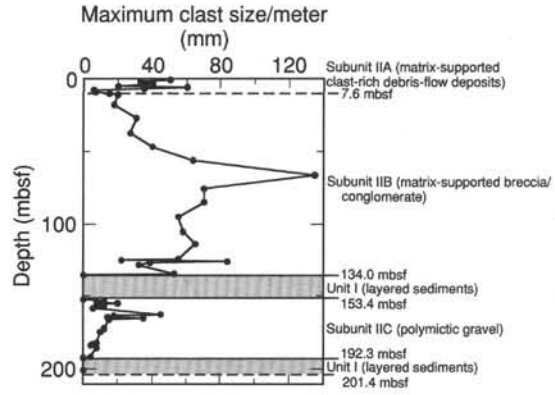

Figure 11. Maximum clast size per meter of recovery from Hole 970A vs. depth. Shaded areas indicate intervals of pelagic sediments where no clasts were recovered.

The presence of these marker species requires a zonal designation of Zone MNN19f.

Samples 160-970B-3H-5, 120 cm, through 4H-2, 77–79 cm, do not contain *Gephyrocapsa* sp. 3 and are dominated by small *Gephyrocapsa.* These samples were placed in Zone MNN19e.

Samples 160-970B-4H-5, 61–63 cm, through 5H-5, 37–39 cm, contain large *Gephyrocapsa* and were placed into Zone MNN19d. Sample 160-970B-5H-CC did not contain large *Gephyrocapsa* and was placed into the next older zone (MNN19c).

Hole 970C

Hole 970C was drilled on the flank of the Milano mud volcano. This location is presumably closer than the other holes to the source of material extruded and eventually transported downslope by gravity-driven flows. Owing to the volume of material emplaced on the slope of the mud volcano by mechanisms other than pelagic rain, most nannofossil assemblages reflect the age of the redeposited material rather than the age of the emplacement event. In fact, Pleistocene nannofossils are rare or absent from all of the samples analyzed.

Because recovery was low, and the composition of all of the cores recovered is similar, the nannofossil samples were prepared only from core-catcher samples and selected clasts. Cores 160-970C-1H, 2H, 3H, and 5X all contain similar assemblages that contain middle Miocene species *Helicosphaera walberdorfensis, C. floridanus, Sphenolithus heteromorphus, Helicosphaera stalis, Calcidiscus premacintyrei,* and medium reticulofenestrids (>8 µm) as the primary constituents. Lesser quantities of *Ericsonia formosa* (lower Oligocene–Eocene) and the Pliocene-Pleistocene species *P. lacunosa* and small *Gephyrocapsa* are also present. Owing to a paucity of in situ pelagic nannofossils, the samples could not be zoned. However, all of the samples contain some specimens attributable to the Pleistocene. Core 160-970C-4X recovered only a single clast that was not analyzed.

Hole 970D

Hole 970D was positioned near the crest of the Milano mud volcano; therefore, the assemblages recovered from the cores at this site reflect a similar proportion of displaced vs. in situ nannofossil assemblages as the samples from Hole 970C. The four cores recovered at this site contain nannofossils similar to those from Hole 970C.

Planktonic Foraminifers

Hole 970A

Planktonic foraminifers were analyzed in all core catchers in addition to samples from within the cores. Both matrix and clast lithol-

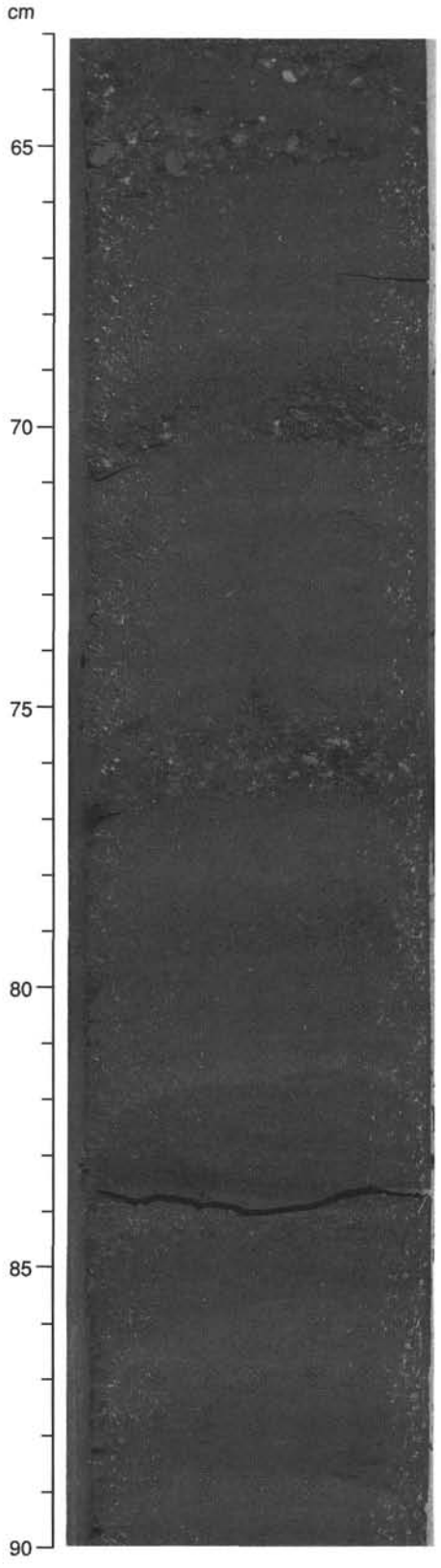

Figure 12. Example of the upward-fining sequences that characterize the polymictic gravel Subunit IIC at Section 160-970A-18X-1, 63–90 cm. (Discontinuities truncating layers are probably caused by rotation and biscuit formation during drilling.)

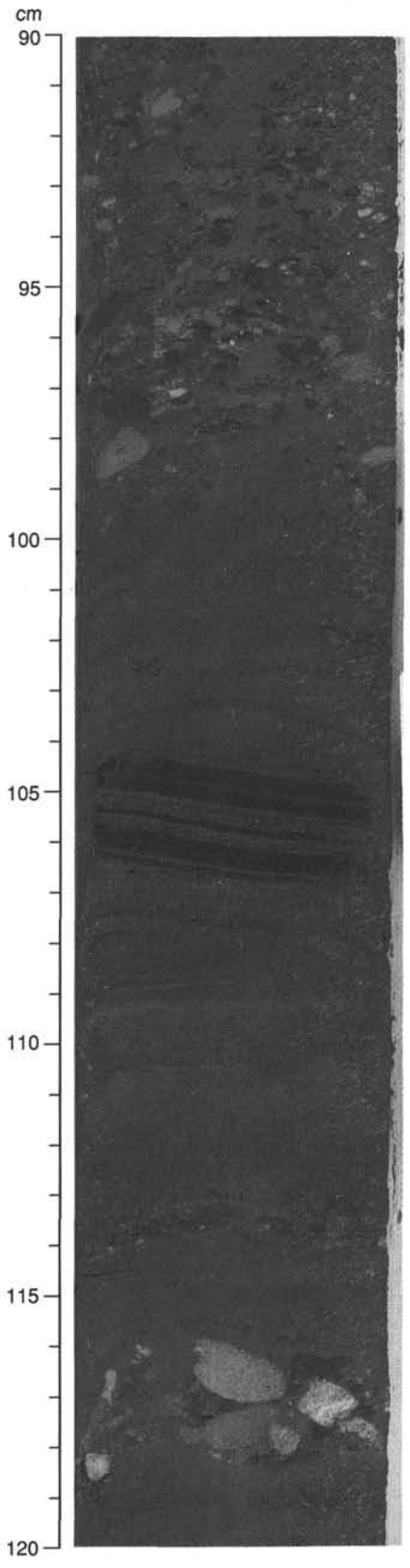

Figure 13. Millimeter-scale graded lamination interbedded with finer grained organic-rich material from 104 to 107 cm in the polymictic gravel Subunit IIC at Section 160-970A-18X-2, 90–120 cm. (Discontinuities truncating layers are probably caused by rotation and biscuit formation during drilling.)

Table 3. Major clast characteristics at Site 970.

Lithology	Size (mm)	Color	Grain size	Sorting	Shape	Carbonate content	Lithification	Hole, core, section, interval (cm)	Comments
Claystone, mudstone	60	Black to dark greenish gray		Well sorted	Angular to subrounded	Noncalcareous	Semiconsolidated	970D-4H-3, 80–86	Homogeneous, some fissility
Claystone, mudstone	30	Dark reddish brown		Well sorted	Subangular to subrounded	Noncalcareous	Semiconsolidated	970C-3H-5, 65–68	Homogeneous
Claystone, mudstone	185	Light greenish gray	Very fine	Well sorted	Subangular to subrounded	Calcareous	Unconsolidated	970D-5H-1, 13.5–32	Homogeneous
Claystone, mudstone	135	Dark greenish gray	Very fine	Well sorted	Subangular to subrounded	Calcareous	Semiconsolidated	970A-9X-1, 46–59.5	Other mud clasts inside
Pelagic limestone	40	Middle gray (N4)	Fine silt to sand	Poorly sorted	Angular to subangular	Calcareous	Well lithified	970A-9X-1, 20–24	Foraminifer-bearing, rarely laminated, and fractured, in part healed with calcite
Siltstone	50	Greenish gray (5GY 4/1)		Well sorted	Subrounded	Calcareous	Well consolidated	970D-4H-5, 62–67	
Siltstone	100	Greenish gray		Well sorted	Subrounded	Calcareous	Semiconsolidated	970D-4H-4, 14–33	
Siltstone	70	Green, white	Coarse to medium silt	Moderately sorted	Angular to subangular	Calcareous	Well lithified	970A-10X-1, 62–69	Lamination on a millimeter scale
Sandstone	50	Dark gray (N5)	Very coarse grained	Moderately sorted	Subrounded	Calcareous	Poorly lithified	970D-3H-6, 45–50	Mudstone clasts inside, darkened fractures
Sandstone	50	Brownish gray	Fine sand grade	Moderately sorted	Subangular	Calcareous	Poorly lithified	970D-3H-5, 101–106	
Sandstone	140	Greenish gray	Medium sand	Well sorted	Rounded to subangular	Calcareous	Semilithified	970D-4H-1, 16–30	Quartz, feldspar, mica, opaque minerals, glauconite, metamorphic rocks, benthic and planktonic foraminifers, and echinoid spines; lamination discernable

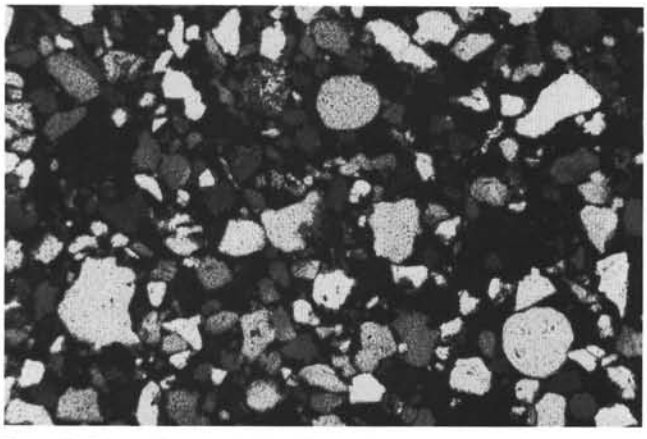

Figure 14. Photomicrograph of a thin section of a sandstone clast from the mud breccias at Section 160-970A-15X-3, 43–45 cm (TSB 172). The variety of grain types and shapes (e.g., quartz shows both very rounded and angular morphologies) suggests multiple sources for the sandstones.

ogies were sampled when simultaneously observed in the mud breccia or when pelagic sediments were recovered. The washed residues generally contain abundant to common quartz, common to rare pyrite, and frequent to rare glauconite, together with planktonic foraminiferal assemblages.

The mud breccia contains reworked and poorly preserved planktonic foraminifers ranging in age from late Oligocene to Pliocene, together with better preserved Pleistocene faunas. Reworked specimens are rare to common whereas Pleistocene specimens are rare to abundant near the transition to pelagic sedimentation.

As previously observed by Staffini et al. (1993) the most common and abundant assemblage observed in the mud breccia comprises the Burdigalian-Langhian (middle Miocene) planktonic faunas *Praeorbulina transitoria, Praeorbulina glomerosa, Globigerinoides bisphericus, Globoquadrina dehiscens, Paragloborotalia acrostoma, Paragloborotalia siakensis, Dentoglobigerina altispira altispira,* and *Dentoglobigerina langhiana.* Present in rare quantities are the Oligocene taxa "*Globigerina*" *ciperoensis* and *Paragloborotalia kugleri* and the Pliocene taxa *Globigerinoides obliquus* and *Globorotalia puncticulata.*

Three intervals of pelagic sedimentation were observed within the mud sequence (Fig. 16). The first (from Cores 160-970A-1H through 3X and Sample 160-970A-4X-1, 84–85 cm), consists of pelagic ooze and is assigned to the Pleistocene *Truncorotalia truncatulinoides excelsa–Globigerina cariacoensis* Zones. Sample 160-970A-4X-1, 84–85 cm, also contains a typical cold-water middle to late Pleistocene assemblage together with abundant *Limacina retroversa* (pteropod). The second interval, located from Cores 160-970A-15X through 17X, is also Pleistocene in age. The third interval is in Core 160-970A-22X and consists of late Pliocene age assemblages. Comparison with the nannofossil data permits its placement in Zone MPL6.

The clasts can be divided into three types. The more common type usually contains assemblages assigned to the Langhian *P. glomerosa* s.l. and *Orbulina suturalis* Biozones (middle Miocene). These consist of the same species observed in the matrix; however, they are much better preserved.

The second and less abundant type of clast contains Eocene morozovellids and acarininids together with rare Oligocene taxa (e.g., *Paragloborotalia pseudokugleri,* "*Globigerina*" *angulisuturalis,* and "*G.*" *ciperoensis*) and the middle Miocene assemblages described above.

The third and least common type of clast consists of gray clay (Sample 160-970A-1H-1, 84–85 cm), and contains a few non-age-diagnostic planktonic foraminifers (e.g., *Turborotalita quinqueloba* and *Globigerinita glutinata*) together with several specimens of ostracodes including possible specimens of *Cyprideis pannonica.*

Hole 970B

Planktonic foraminifers were analyzed in all core catchers in addition to samples from within the cores (Fig. 16). The pelagic sedi-

ments contain Pleistocene planktonic foraminiferal assemblages similar to those observed at Sites 963 through 969. They consist of common *Orbulina universa, Globigerinoides ruber, Globigerinoides elongatus, Globigerinoides gomitulus, Globorotalia inflata, Globorotalia scitula, Globigerina bulloides, Globigerina falconensis, G. glutinata, Globigerinita juvenilis, Globigerinella siphonifera,* and *Turborotalita quinqueloba.* Rarer are *Orbulina bilobata, Globigerinoides pyramidalis, G. gomitulus, G. conglobatus,* and *Globigerina calida.* Very rare are the taxa *Hastigerinopsis riedeli* and *Hastigerina parapelagica.* Reworking occurs sporadically in Hole 970B and consists of rare specimens of *Globorotalia crassaformis* and *G. obliquus.*

Holes 970C and 970D

Only the core catchers of the five cores recovered from Hole 970C and 970D were studied. They all contain the mud breccia previously observed at Hole 970A. No substantial differences were observed concerning the matrix and clasts. The matrix usually contains a Burdigalian-Langhian assemblage together with rarer Eocene, Oligocene, and Pliocene taxa. The clasts contain early Langhian assemblages or alternatively Eocene, Oligocene, and middle Miocene age assemblages.

PALEOMAGNETISM

Owing to the disturbed nature of the sediment recovered from Site 970 at the Milano mud volcano, detailed paleomagnetic studies were not attempted. Sections from Cores 160-970A-1H and 2H (0–10 mbsf) were measured on the shipboard pass-through cryogenic magnetometer after AF demagnetization at 25 mT in order to assess the possibility of using paleomagnetic data to resolve structural features or to distinguish between different mud flows. Paleomagnetic inclination, intensity, and magnetic susceptibility are shown in Figure 18.

Two textural changes are evident in Cores 160-970A-1H and 2H, with the upper lithology comprising a pelagic mud, followed by matrix-supported clast-rich debris-flow deposits, and the lower lithology consisting of a matrix-supported breccia/conglomerate (see "Lithostratigraphy" section, this chapter). These three sediment units are well delineated by remanence intensity changes at 0.5 and 7.6 mbsf, respectively. However, these changes are not evident in the magnetic susceptibility record (Fig. 18). The textural change at 7.6 mbsf may indicate the presence of two different mud-flow units. Paleomagnetic inclination data (Fig. 18) are variable throughout the 10-m interval on which measurements were made. The high-amplitude inclination variations in the upper 6.5 m may be caused by the presence of gravel clasts that compete with the magnetization of the mud matrix to produce an incoherent signal. However, at about 6.5 mbsf (within Section 160-970A-1H-5), a marked change from reverse to normal polarity was recorded, whereas variable normal polarity directions occur from 6.5 to 10 mbsf. This change in polarity occurs within the lowermost section of Core 160-970A-1H. It is possible that the polarity change at 6.5 mbsf may reflect a boundary between flows, if the lower part of the uppermost flow was overturned during emplacement. Such an interpretation would require viscous flow in which the magnetization of the material is already locked in at the time of final emplacement of the flow. Alternatively, the polarity change could also be caused by coring an unrecognized large mud clast that was overturned after acquiring its remanence. These interpretations are speculative and would require confirmation from another source. The paleomagnetic data otherwise shed little light on the process of mud-flow emplacement.

INORGANIC GEOCHEMISTRY

Interstitial-water samples were obtained at Site 970 from Holes 970B, 970A, 970C, and 970D, which constitute a transect from the

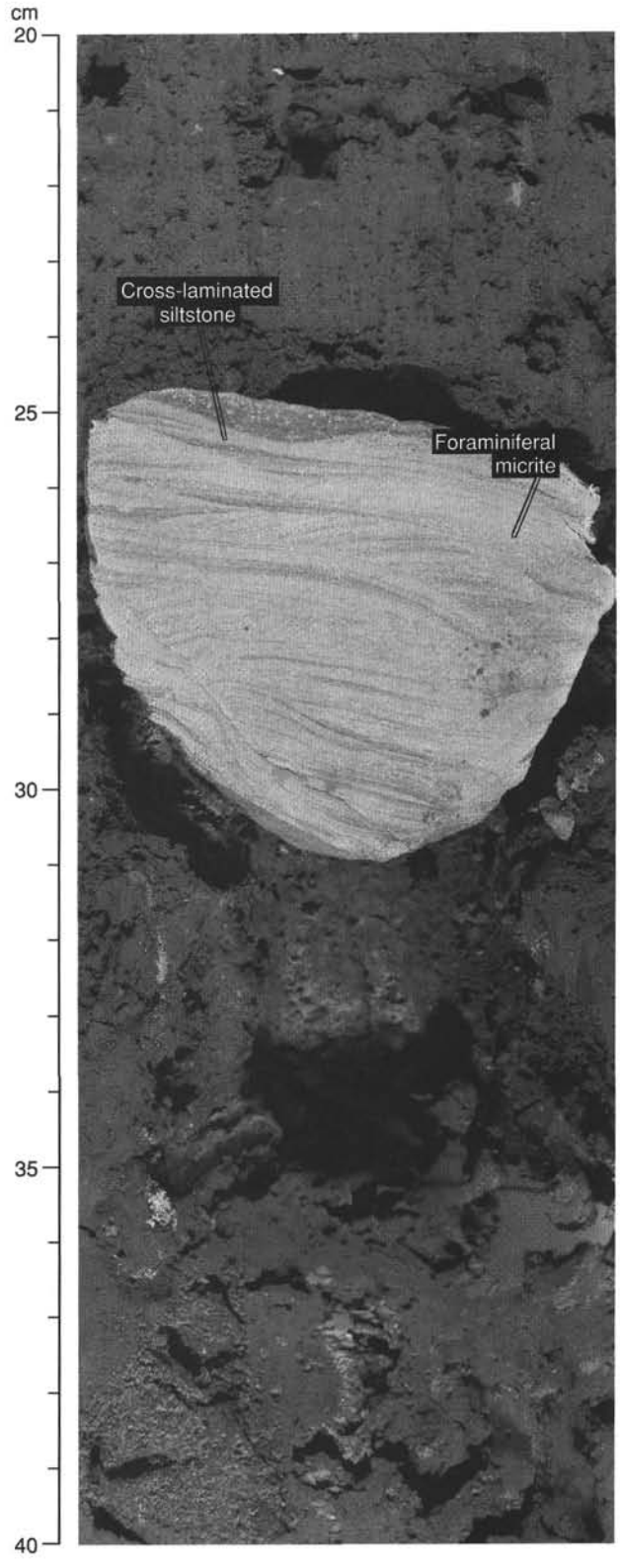

Figure 15. Photograph of a ripple cross-laminated siltstone, in contact with planktonic foraminiferal micrite within matrix-supported clast-rich debris-flow deposits (Subunit IIA) at Section 160-970C-1H-4, 20–40 cm.

Table 4. Structural data collected at Site 970.

Core, section, interval (cm)	Depth (mbsf)	Feature	Offset (cm)	Orientation on core face (degrees)		Second apparent orientation (degrees)		Calculated orientation (degrees)		Geographic orientation (degrees)		Comments
				Apparent dip	Direction	Apparent dip	Direction	Dip	Direction	Dip	Direction	
160-970A-												
16X-1, 23–26	134.2	F	1.4	45	270	8	0	45	278			Normal
16X-2, 94–110	136.4	B		80	270	0	48	83	318			Pyrite lined, vertical in places
17X-3, 29–31	146.9	F	1.5	21	270	0	12	21	282			Slightly reverse
17X-4, 38–40	148.5	f	0.3	22	90	35	0	39	30			?Reverse
160-970B-												
2H-3, 133–138	11.96	SB		42	90	12	0	43	77			
2H-3, 139	12.02	SB		4	90	9	0	10	24			
2H-4, 33–40	12.42	SB		28	270	30	0	38	317			Geochemical front
2H-4, 40–41	12.49	SB		12	270	34	0	35	343			Geochemical front
2H-4, 65–66	12.74	SB		11	270	5	180	12	246			Geochemical front
2H-5, 16	13.63	SB		6	270	11	180	12	208			Yellow band
2H-5, 18	13.65	SB		8	270	16	180	18	206			Yellow band
2H-5, 46–49	13.93	SB		17	90	2	180	17	96			Thin organic-rich layer
2H-5, 82	14.29	SB		0	90	7	0	7	0			Top of organic-rich layer
2H-6, 68–70	15.6	SB		11	270	9	0	14	309			Top of organic-rich layer
2H-6, 107–108	15.99	SB		7	270	7	0	10	315			Geochemical front
2H-7, 32–33	16.64	SB		9	90	9	0	13	45			Foraminifer sand
2H-8, 29	18.04	SB		0	90	0	0	0	0			Geochemical front
4H-1, 34	28.84	SB		2	270	6	0	6	342	6	198.5	Color change
4H-1, 74–80	29.24	DIS		54	270	40	0	58	301	58	157.5	Top of mud clast
4H-1, 101	29.51	SB		0	90	16	0	16	0	16	216.5	
4H-1, 136–143	29.86	DIS		34	90	10	180	35	105	35	321.5	Sharp contact at base of debris flow
4H-2, 47–48	30.47	SB		6	90	2	0	6	72	6	288.5	Yellow band
4H-3, 122–124	32.72	SB		12	90	0	0	12	90	12	306.5	
4H-3, 138–139	32.88	SB		8	90	9	180	12	138	12	354.5	
4H-4, 70–70	33.7	SB		0	90	20	0	20	0	20	216.5	Sand
4H-4, 131–131	34.31	SB		11	270	2	0	11	280	11	135.5	
4H-4, 138–146	34.38	F	2	57	90	0	334	60	64	60	280.5	Normal
4H-5, 77–82	35.27	SB		45	90	30	0	49	60	49	276.5	Within green clast
4H-6, 80–82	36.8	SB		11	270	11	180	15	225	15	81.5	
4H-6, 100–102	37	SB		9	270	3	180	9	252	9	108.5	
5H-1, 50–51	38.5	SB		3	270							Bottom of organic-rich layer
5H-1, 82–83	38.82	SB		6	270							Top of organic-rich layer
5H-2, 115	40.38	SB		7	270	15	180	16	205	16	24.5	
5H-2, 115–121	40.38	F	0.5	62	270	0	34	66	304	66	123.5	Normal
5H-2, 120–125	40.43	F	1	60	270	0	28	63	298	63	117.5	Normal
5H-3, 81–85	41.54	F		60	90	0	62	75	152	75	331.5	
5H-3, 83–86	41.56	F		70	270	0	324	74	234	74	53.5	
5H-3, 107–113	41.8	F	>6	30	90	41	180	46	146	46	325.5	
5H-4, 9–28	42.32	F	6	80	270	Not visible						Reverse fault
5H-5, 76–76	44.49	SB		4	90	18	0	18	12	18	191.5	
5H-5, 93–102	44.66	DIS		60	270	0	292	78	202	78	21.5	
5H-5, 95–105	44.68	DIS		58	270	0	313	77	223	77	42.5	

Note: Feature symbols defined in Table 2 ("Explanatory Notes" chapter, this volume).

rim toward the crest of the Milano mud volcano. The standard ODP titanium/stainless-steel squeezer (Manheim and Sayles, 1974) and a plastic-lined squeezer (Brumsack et al., 1992) were used for pore-water squeezing. In total, 21 samples covering a depth range from 1.27 to 194.5 mbsf were retrieved and subsequently analyzed for salinity, alkalinity, chloride, sulfate, lithium, potassium, calcium, magnesium, ammonium, and silica using the methods described in the "Explanatory Notes" chapter (this volume). In contrast to the previous site reports, we discuss the individual holes of Site 970 in this section because their fluid regimes and therefore pore-water chemistries differ substantially (Table 5).

Hole 970B

Hole 970B, located at the outer rim of the Milano mud volcano, is characterized by a relatively steep increase in salinity, which leads to chloride and potassium values at 43.63 mbsf that are more than twice the seawater values (Fig. 19). By extrapolation of the gradients, the presence of an evaporite brine may be postulated at a depth of not more than 200 to 250 mbsf. The increasing concentrations of sodium and chloride are paralleled by increases in potassium and lithium that also seem to be related to the presence of a brine at greater depth.

Although the sulfate profile does not show any evidence of bacterial sulfate reduction, alkalinity values are higher than bottom-water concentrations, which suggests that organic matter is degraded in this hole (Fig. 20). This assumption is supported by a steady increase in the ammonium concentration from 200 μM in the uppermost sample to almost 600 μM at the bottom of this hole (Fig. 20). The negative excursion in the alkalinity profile suggests that carbonate precipitation is taking place, though this is not reflected in the calcium and magnesium profiles (Fig. 21). The generally increasing concentrations of both these elements with depth suggest that they are diffusing upward from deeper downhole, as seems to be the case for the alkali metals (Fig. 21). The increase seen in the sulfate concentration for the two lower samples implies a source for this ion at depth, too, possibly evaporite brine and associated gypsum deposits.

Silica levels are almost constant and low at this hole (Fig. 20), which suggests equilibrium with clay minerals and/or quartz. Amorphous silica phases do not seem to be present in large quantities.

Hole 970A

Hole 970A was drilled on the slope of the Milano mud volcano. Unfortunately, only two samples from the top of the hole (5.90 and 8.95 mbsf) and seven samples from greater depth (135.35 to 194.50 mbsf) were obtained. For the intervening depth interval within the mud breccias, pore waters could not be obtained because of poor recovery.

The steep increase in the salinity profile below 150 mbsf is reflected in the sodium and chloride profiles (Fig. 22). Similar concen-

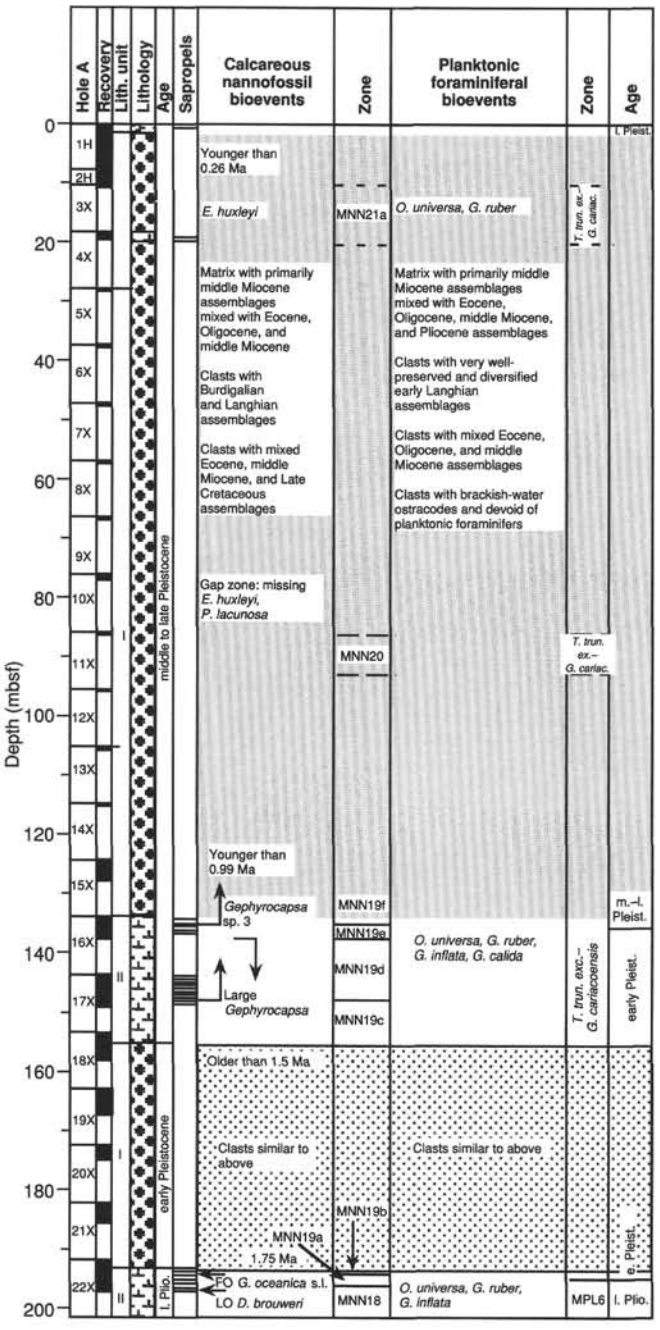

Figure 16. Composite of biostratigraphic events recognized in the sediments recovered from Hole 970A including the lithostratigraphic record.

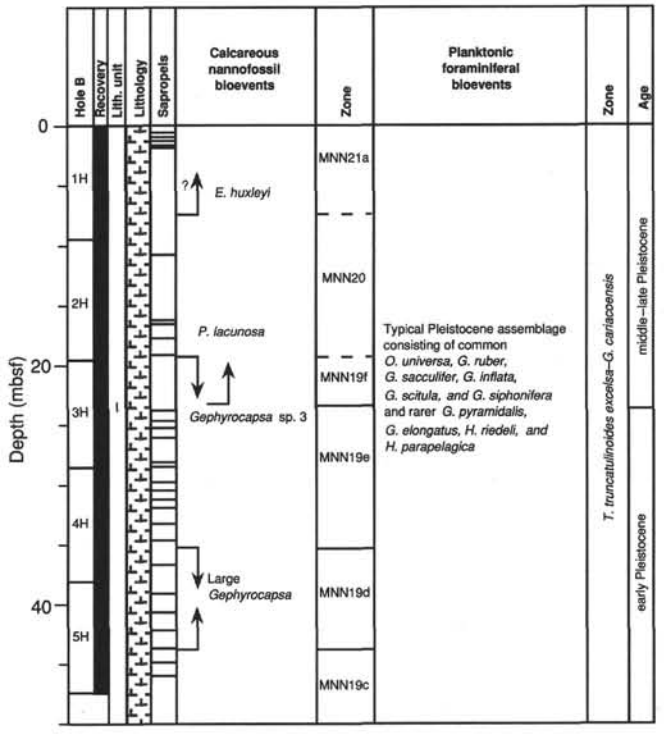

Figure 17. Composite of biostratigraphic events recognized in the sediments recovered from Hole 970B including the lithostratigraphic record.

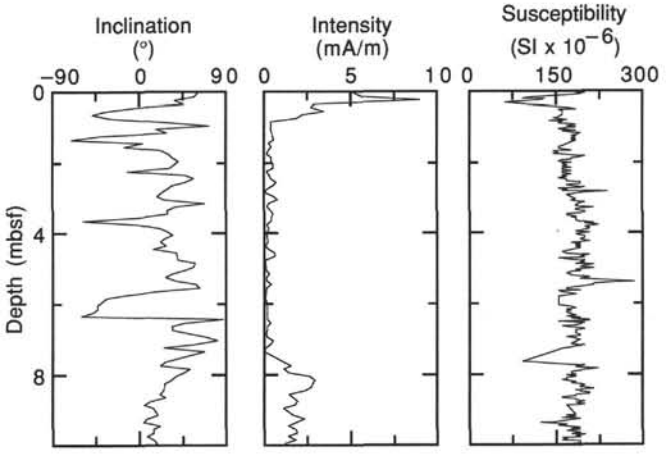

Figure 18. Paleomagnetic inclination, intensity, and magnetic susceptibility for Hole 970A. Inclination and intensity were measured after AF demagnetization at 25 mT.

tration profiles were obtained for lithium and potassium in the lower part of this hole (Fig. 23). Sulfate concentrations are close to Mediterranean seawater values at the top of the hole, drop to values of 17.3 mM at 135.35 mbsf, and then start to increase again. This increase may be caused by supply of sulfate from deeper downhole (Fig. 24).

The abrupt increase in ammonium concentrations in the top of the hole (Fig. 24) indicates organic matter degradation, possibly within the breccia/conglomerate of Subunits IIA and IIB (see "Lithostratigraphy" section, this chapter). This assumption is supported by the ammonium gradients below Subunit IIB, which imply an ammonium source above and below 170 mbsf.

Calcium and magnesium values decrease from seawater values in the uppermost two samples (Fig. 23). Below Subunit IIB both elements show an increase similar to chloride, indicating supply from below. Comparably low alkalinity and sulfate levels, as well as higher ammonium concentrations, suggest that carbonate precipitation reactions are occurring (Fig. 24), although they are masked by the diffusive supply of alkaline earth elements from the evaporate brine located below.

Silica concentrations are low throughout the hole and decrease in the polymictic gravel of Subunit IIC. Decreasing silica gradients also occur in the matrix-supported clast-rich debris-flow deposits of Sub-

Table 5. Results of pore-water analysis for Site 970.

Core, section, interval (cm)	Depth (mbsf)	pH	Alkalinity (meq/L)	Salinity (g/kg)	Cl^- (mM)	Mg^{2+} (mM)	Ca^{2+} (mM)	SO_4^{2-} (mM)	NH_4^+ (μM)	SiO_2 (μM)	K^+ (mM)	Li^+ (μM)	Na^+ (mM)
160-970A-													
1H-4, 140–150	5.90	7.81	3.615	37.0	606	57.0	11.4	31.49	410	156	9.8	58.0	524
2H-1, 135–150	8.95	7.77	3.352	37.8	607	54.1	10.1	31.15	575	139	7.6	69.0	554
16X-1, 135–150	135.35	7.47	2.528	47.7	813	56.4	16.0	17.30	911	191	10.5	54.0	665
17X-1, 135–150	144.95	7.43	2.279	50.0	844	60.0	17.9	17.33	821	209	11.6	53.0	724
18X-2, 135–150	155.85	—	—	56.5	932	74.2	24.1	19.51	669	214	12.1	55.0	771
19X-2, 123–138	165.53	—	—	64.6	1103	88.7	29.6	21.65	652	179	15.2	61.0	933
20X-1, 135–150	173.85	7.58	2.299	72.4	1266	97.3	33.4	26.72	650	139	17.5	65.5	1000
21X-2, 95–115	184.55	—	—	89.5	1529	100.6	39.0	28.71	715	154	19.4	73.0	1322
22X-2, 130–150	194.50	7.70	1.035	99.0	1715	94.3	36.9	30.62	1032	90	27.8	75.5	1601
160-970B-													
1H-4, 140–150	5.90	7.29	3.691	48.0	794	69.7	15.4	31.11	208	156	15.5	43.0	705
3H-4, 140–150	24.90	7.30	2.433	69.0	1159	83.1	21.8	30.99	383	152	20.9	52.0	1087
4H-5, 140–150	35.90	7.30	2.379	80.0	1373	80.8	22.6	32.80	484	166	21.6	55.5	1238
5H-4, 140–150	43.63	7.19	3.179	89.5	1537	83.5	25.8	34.48	573	141	24.9	60.0	1434
160-970C-													
1H-2, 145–150	2.95	—	—	28.7	509	18.7	1.6	0.66	1054	380	4.61	42.0	478
2H-2, 132–142	7.52	—	—	22.0	369	2.4	0.6	0.54	1164	226	1.24	29.5	420
3H-2, 0–10	9.70	—	—	20.3	350	2.0	0.5	0.58	1124	195	0.92	31.5	375
160-970D-													
1H-1, 127–150	1.27	8.61	39.461	11.7	183	1.6	0.4	0.8	734	181	0.60	17.0	223
2H-5, 130–150	12.10	—	—	12.5	202	1.2	0.5	0.2	693	205	0.80	23.0	251
3H-6, 130–150	23.10	8.55	48.127	14.8	236	1.7	0.0	0.3	686	181	0.90	28.5	273
4H-5, 130–150	30.71	8.70	72.451	7.0	61	0.7	0.0	0.1	456	246	0.30	16.5	131
5H-6, 130–150	41.80	8.39	69.461	9.9	88	0.6	0.0	0.5	759	201	0.60	16.0	162

Note: — = no data.

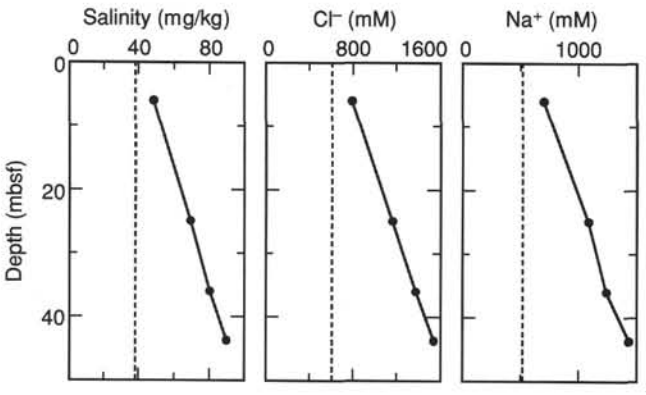

Figure 19. Pore-water vs. depth profiles at Hole 970B for salinity, chloride, and sodium. The dashed line indicates the bottom-water concentration.

unit IIA (Fig. 24), which suggests that the mud volcano deposits are devoid of any amorphous silica phases.

Holes 970C and 970D

Both holes from the crestal part of the Milano mud dome are characterized by salinity, chloride, and potassium values below those of contemporaneous Mediterranean bottom water (Fig. 25). Salinity, chloride, and sodium values decrease to less than two-thirds of seawater levels in Hole 970C and only 11% seawater in Hole 970D. The fluids are very low in sulfate (less than 0.8 mM in all samples retrieved) and high in ammonium and alkalinity (Fig. 26), which indicates that the zone of active bacterial sulfate reduction is restricted to the upper few meters in both holes. The sulfate source must be seawater, which diffuses down from the sediment/seawater interface.

In accordance with the high alkalinity buildup, carbonate seems to be precipitated close to, or at, the sediment surface, because the calcium and magnesium concentrations are far below seawater values (Fig. 27). In Hole 970C, values for magnesium and calcium are higher in the uppermost sample recovered (2.95 mbsf), which indicates that the fluids from deeper downhole are essentially free of alkaline earth elements.

The alkali metals lithium and potassium (Fig. 27) display different behaviors in the two holes. Whereas the lithium concentration is much higher than seawater at Hole 970C, its concentration is distinctly lower at Hole 970D. This difference may result from the higher degradation rate of organic matter, as reflected in higher ammonium concentrations, in Hole 970C. A similar increase was not seen for potassium (Fig. 27).

The silica concentrations are also different in the uppermost samples of both holes. Whereas a distinct increase is discernible in the uppermost samples from Hole 970C, silica values are almost constant in Hole 970D (Fig. 26). In the latter hole, the silica concentrations are close to the values expected for equilibrium with clay minerals and/or quartz. By contrast, in Hole 970C a significant contribution from the dissolution/transformation of amorphous silica phases in the uppermost section is likely.

In both Holes 970C and 970D, the composition of the pore waters below 7.52 mbsf is rather similar. This is also evident when the ratios of sulfate, potassium, and lithium to chloride are plotted vs. depth (Fig. 28). It should be noted that in Hole 970D two different solutions appear to be present, because there is a significant change in the composition above and below the interval from 23.10 to 30.71 mbsf.

Causes for the Presence of Low-salinity Pore Waters at Milano Dome

The presence of low-salinity waters in an environment that is characterized by the involvement of evaporites in the pore-fluid regime is quite puzzling. Two explanations are possible: (1) expulsion of low-salinity waters from sources deeper downhole and (2) presence of significant amounts of methane clathrates.

The first possibility seems rather unlikely from a geological point of view, because large parts of the Mediterranean seafloor are covered by Messinian evaporites. Not a single site drilled in the Mediterranean is characterized by a significant decrease in salinity at greater depth. By contrast, steep increases in salinity were found at most sites. Furthermore, mixing of fresh waters and seawater would not result in a significant change of element/chloride ratios from seawater values, as is the case in Holes 970C and 970D (Fig. 28).

The second possibility is strongly supported by the presence of large amounts of methane in the vacutainer and headspace samples (see "Organic Geochemistry" section, this chapter). Unfortunately,

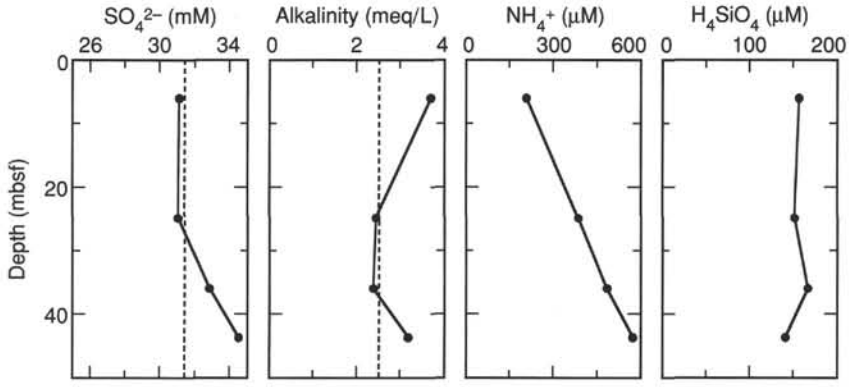

Figure 20. Pore-water vs. depth profiles at Hole 970B for sulfate, alkalinity, ammonium, and silica. The dashed line indicates the bottom-water concentration; the ammonium bottom-water concentration is <1 µM.

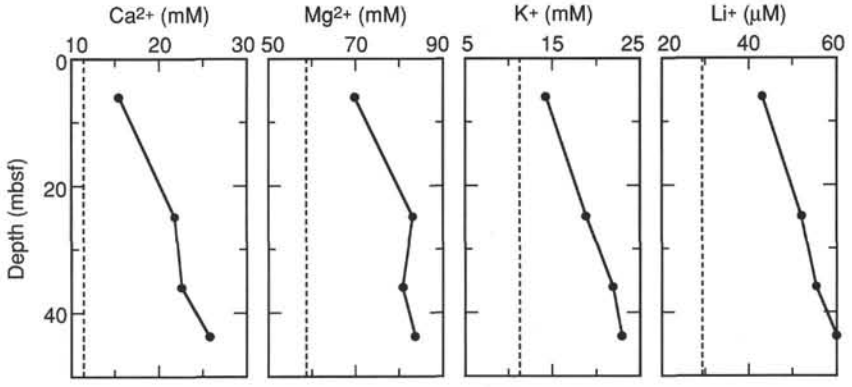

Figure 21. Pore-water vs. depth profiles at Hole 970B for calcium, magnesium, potassium, and lithium. The dashed line indicates the bottom-water concentration.

gas hydrates were not recovered in both holes, because they easily decompose upon retrieval of the cores. Nevertheless, the presence of clathrates close to the sediment/seawater interface in Hole 970D can be postulated. This assumption is supported by the extremely low salinity values encountered at this hole. Values as low as 7 g/kg can be explained only by the contribution to the pore-water pool of at least 80% hydrate water and of less than 20% pore water of "normal" Mediterranean bottom water with a salinity of 38 g/kg. Sulfate is essentially absent below 1.3 mbsf, and alkalinity values of more than 70 mM reflect the bacterial consumption of methane.

In Hole 970C, the clathrate layer seems to be located at a slightly greater depth and most likely was just penetrated by drilling. The Milano mud volcano represents one of the few deep-sea areas where gas hydrates are accessible by piston coring. The formation of methane clathrates directly at or just below the sediment/seawater interface seems to be related to the high supply rate of methane by emanating fluids, the pressure (water depth) and temperature of the bottom water (about 14°C), and the availability of pore space (mud breccia). All these prerequisites are accomplished at Hole 970D and perhaps at Hole 970C, and seem to be compatible with the stability field of methane gas hydrates.

ORGANIC GEOCHEMISTRY

Volatile Hydrocarbons

As part of the shipboard safety and pollution-prevention monitoring program, hydrocarbon gases were analyzed in each core of Holes 970A through 970D by the headspace technique and, where gas pockets occurred, also using vacutainer gas samples. Only minor concentrations of methane in the range of 2 to 15 ppm were recorded in Holes 970A and 970B. In Hole 970C, headspace analysis yielded almost 5000 ppm of methane in the first core and about 2000 ppm of methane in Cores 160-970C-2H and 3H. A vacutainer sample from

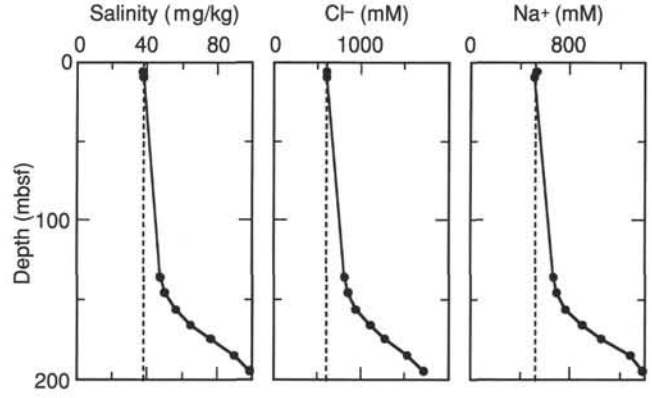

Figure 22. Pore-water vs. depth profiles at Hole 970A for salinity, chloride, and sodium. The dashed line indicates the bottom-water concentration.

Core 160-970C-2H contained almost 14,000 ppm of methane (Table 6). Ethane was absent or present only in trace amounts in all of these samples.

Gas was abundant in Hole 970D on the crest of the Milano mud volcano and produced visually obvious core expansion features such as abundant gas pockets and the rupture of the core liner of Core 160-970D-2H. Methane concentrations in the gas pockets increased from about 500,000 ppm in Core 160-970D-1H to 1,000,000 ppm (corresponding to pure methane at ambient pressure) in Core 160-970D-3H (Table 6, Fig. 29A) and then decreased again by almost 2 orders of magnitude in Core 160-970D-5H. At the same time, the concentrations of higher hydrocarbons relative to methane increased toward the bottom of the hole (Table 6), and the methane/ethane ratio decreased from about 1280 in the shallowest core to 18 in Core 160-970D-5H (Fig. 29A). Headspace-gas analysis yielded compatible re-

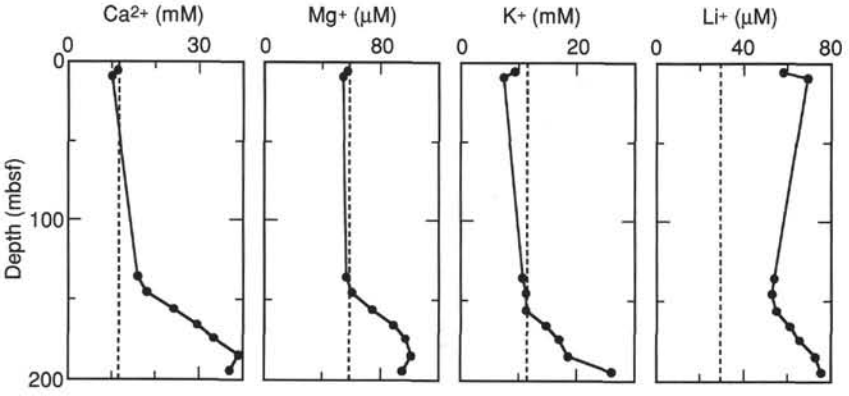

Figure 23. Pore-water vs. depth profiles at Hole 970A for calcium, magnesium, potassium, and lithium. The dashed line indicates the bottom-water concentration.

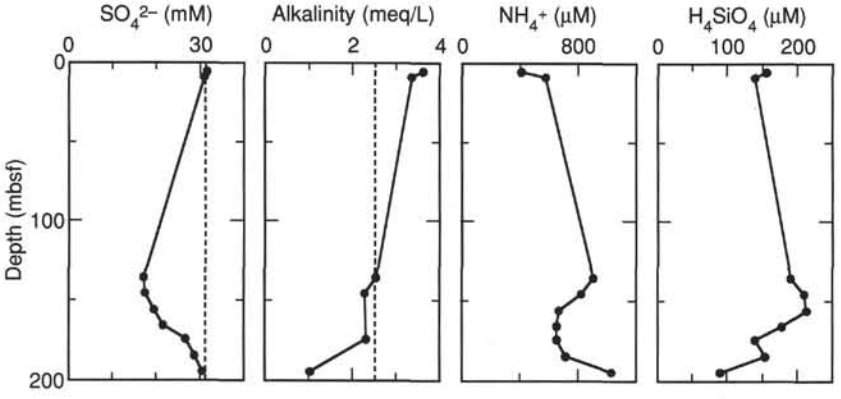

Figure 24. Pore-water vs. depth profiles at Hole 970A for sulfate, alkalinity, ammonium, and silica. The dashed line indicates the bottom-water concentration.

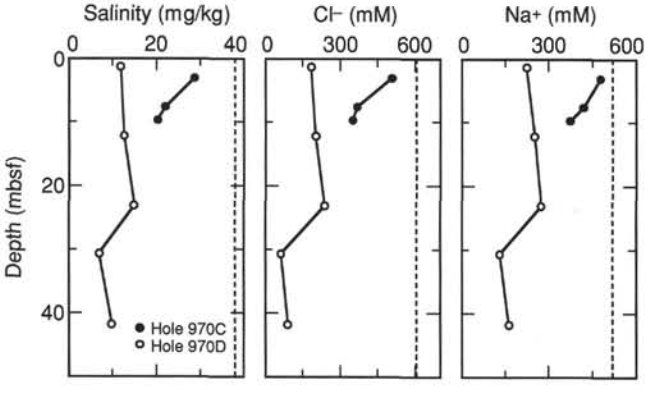

Figure 25. Pore-water vs. depth profiles at Holes 970C and 970D for salinity, chloride, and sodium. The dashed line indicates the bottom-water concentration.

sults but lower absolute concentrations, corresponding to the type of analysis (Table 6, Fig. 29); the methane/ethane ratio showed a trend similar to that of the vacutainer gas (Fig. 29).

The gas profile in Hole 970D can be explained by the presence of methane clathrates in the top few tens of meters of the sediment. Water depth and an estimated bottom-water temperature of about 14°C are compatible with the stability field of methane gas hydrates (Katz et al., 1959). Relative enrichment of higher hydrocarbons and a decrease of absolute methane concentrations with increasing depth are both consistent with the selective removal of methane because of clathrate formation in the shallower part of the section. In contrast to this, the low concentrations of ethane in the sediments from Hole 970C at an almost constant level of headspace methane may indicate that the clathrate zone was not penetrated. The absence of abundant gas pockets in Core 160-970C-3H and the relatively low methane concentration in the vacutainer sample from Core 160-970C-2H are probably evidence of lower clathrate abundance than in Hole 970D.

Carbonate and Organic Carbon

The abundances of total, inorganic, and organic carbon and of calcium carbonate in sediments from Holes 970A through 970D are summarized in Table 7.

The carbonate content in the pelagic sections of Holes 970A and 970B mostly varies between 40% and 60% except for some sapropels in Cores 160-970A-22X and 160-970B-4H and 5H, which contain less than 25% carbonate. The shallower sapropels in both holes cannot be distinguished from pelagic background sediment based on carbonate content (Table 7, Fig. 30). Mud-flow sections in Holes 970A, 970C, and 970D typically contain about 15% carbonate with the exception of the deeper mud-flow unit in Hole 970A, which is distinguished from the others by a slightly higher carbonate content of 20%–30% (Table 7).

Organic carbon was determined mainly for sediments visually distinguished by their dark colors. Sapropels in the pelagic sections contain more than 2% organic carbon and reach values as high as 23% in Cores 160-970A-22X and 160-970B-4H and 5H. Typical organic carbon content values of the mud-flow sediments are close to 0.5% (Table 7, Fig. 30).

Organic Matter Type: C_{org}/N Ratios and Rock-Eval Pyrolysis

C_{org}/N ratios for all sapropels exceed the value of 12; they have an average ratio of 17 and a maximum of 21.7 (Table 7). As already observed for sapropels at previous sites (see, "Organic Geochemistry" section, chapters for Sites 964 and 966–969, this volume), the surprisingly high values of the C_{org}/N ratio in many of the sapropels sug-

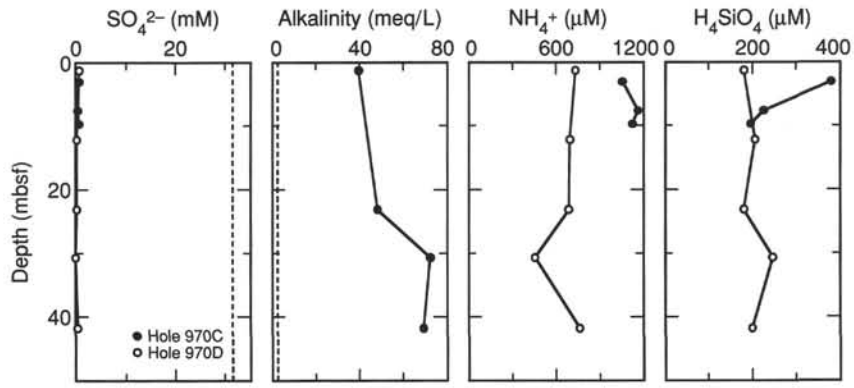

Figure 26. Pore-water vs. depth profiles at Holes 970C and 970D for sulfate, alkalinity, ammonium, and silica. The dashed line indicates the bottom-water concentration; the ammonium bottom-water concentration is <1 µM.

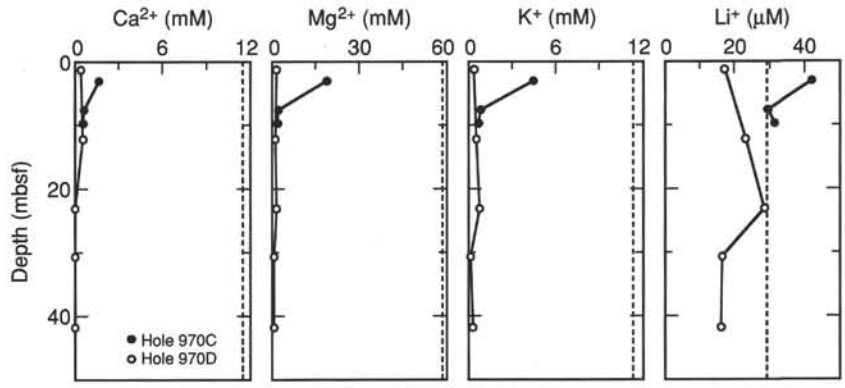

Figure 27. Pore-water vs. depth profiles at Holes 970C and 970D for calcium, magnesium, potassium, and lithium. The dashed line indicates the bottom-water concentration.

gest a predominance of terrestrial organic matter, which is not in accordance with the indications provided by the Rock-Eval parameters. The high C_{org}/N ratios in the sapropels are again interpreted as representing an effective removal of nitrogen compounds from the marine organic matter during diagenesis. The primary C_{org}/N ratios of the mud-flow sediments with organic carbon contents below 0.8% are mostly below 10, which indicates that inorganic nitrogen may have contributed to the measured nitrogen values.

Results of Rock-Eval pyrolysis (Table 8) show hydrogen indices for several sapropel samples to exceed 300, with a maximum value of 378 measured in Core 160-970A-22X. The hydrogen index values indicate partial oxidation of the primary marine organic matter with the formation of inert micrinite and/or an admixture of terrigenous organic matter. The former explanation is favored because the oxygen indices are low throughout.

Sulfur

Sulfur contents are reported in Table 7. With some exceptions in Core 160-970B-2H, they are higher than 2% in sapropels, with a maximum of 12.9% in Sample 160-970B-4H-5, 8–9 cm. Most of the sulfur is present as pyrite because pyrite concretions were visually detected in the sapropels and abundant disseminated pyrite was observed under the microscope. For most sapropels there is a tendency for covariation of the sulfur and organic carbon contents.

PHYSICAL PROPERTIES

A complete suite of physical properties (see "Explanatory Notes" chapter, this volume) was measured in all cores recovered from Hole 970A, and index properties were measured in cores recovered from Holes 970B through 970D.

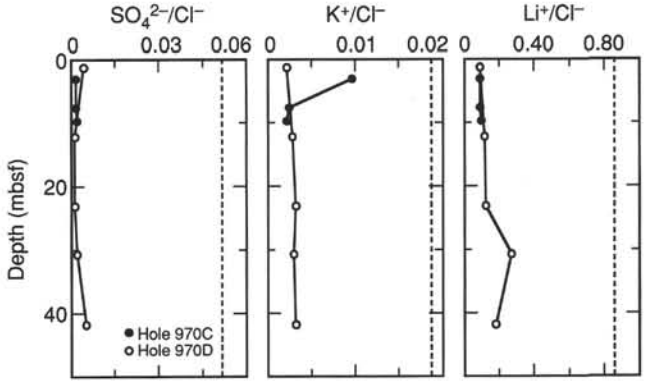

Figure 28. Pore-water vs. depth profiles at Holes 970C and 970D for sulfate/chloride, potassium/chloride, and lithium/chloride ratios. The dashed line indicates the bottom-water value.

Index Properties

Index properties measurements are contained in Table 9 and shown in Figures 31 and 32. To a first approximation, the index properties appear to be lithologically controlled (see "Lithostratigraphy" section, this chapter, for detailed descriptions of the lithologies referred to below). In Hole 970A, the uppermost 7.6 m contained primarily matrix-supported clast-rich debris-flow deposits, and this lithology corresponds to an interval of increasing bulk density, decreasing porosity, and approximately constant grain density. These deposits are the sole lithology in Holes 970C and 970D, but index properties trends differ in these two holes. In Hole 970C, porosity decreases and bulk density increases with depth, but grain density

Table 6. Hydrocarbon gas data for Site 970, headspace method and Natural Gas Analyzer.

Core, section, interval (cm)	Depth (mbsf)	C_1 (ppm)	C_2 (ppm)	C_3 (ppm)	i-C_4 (ppm)	n-C_4 (ppm)	i-C_5 (ppm)	n-C_6 (ppm)	C_1/C_2	Method
160-970C-										
1H-3, 0–5	3.00	4,915	3						1638	H
2H-2, 50–51	6.70	13,883	3						4628	V
2H-2, 127–132	7.47	2,056								H
3H-1, 145–150	9.65	2,111								H
160-970D-										
1H-2, 0–5	1.50	3,918	5						784	H
1H-2, 50–51	2.01	538,545	422	4	2	3			1280	V
2H-4, 0–5	9.30	3,156	3						1052	H
3H-3, 50–51	17.80	1,000,000	1017	9		5		1	986	V
3H-4, 0–5	18.80	4,548	40						114	H
4H-3, 0–5	26.41	3,131	140	5					22	H
4H-3, 50–51	26.91	205,849	1715	14	25	1	3		120	V
5H-3, 0–5	36.00	2,103	229	12					9	H
5H-3, 50–51	36.50	19,577	1082	36	11		2		18	V

Note: H = headspace; V = vacutainer.

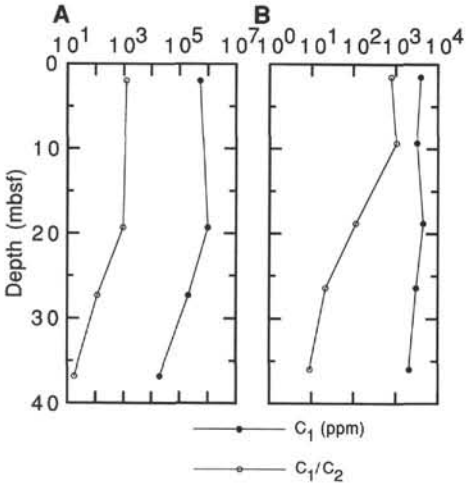

Figure 29. Downhole variation of methane concentrations and methane/ethane (C_1/C_2) ratios for (**A**) vacutainer samples and (**B**) headspace samples from Hole 970D.

shows a rhythmic variation on the scale of a few meters. This may result from variations in clast size and lithology, because a wide variety of clast types was found in the mud matrix. In contrast to the other holes containing the matrix-supported clast-rich debris-flow deposits, bulk density decreases and porosity increases in the upper 5 m of Hole 970D. Below 5 mbsf, bulk density, grain density, and porosity are approximately constant in Hole 970D. The constant density and porosity below 5 mbsf may be caused by gas pressure from below inhibiting the normal compaction of sediments in this hole.

The second lithology related directly to mud volcanism is a matrix-supported breccia/conglomerate, which was found at 7.6–134 mbsf in Hole 970A. Poor core recovery in this interval precludes definitive statements about the relationship of index properties to lithology. However, data from one interval of this lithology that had better than average recovery (Core 160-970A-15X) show considerable variability in density and porosity (Figs. 31, 32); such variability is consistent with the heterogeneous nature of this lithostratigraphic unit.

The stratigraphically lowest lithostratigraphic unit related to the mud volcano, which was found between 153 and 192 mbsf in Hole 970A, is described as a polymictic gravel with several fining-upward sequences. Core recovery in this interval was approximately 40%, and the index properties density data show a series of apparent step-like increases (Figs. 31, 32). This is an effect of low core recovery resulting in the concentration of the natural variance of values that occurs over 9.5 m in the upper 20–30 cm of the core section.

The mud volcano sediments are interlayered with and overlain by pelagic nannofossil ooze with sapropels. This is the only sediment type found in Hole 970B, and density and porosity in this hole generally show an increase and a decrease, respectively (Figs. 31, 32), which is consistent with the effects of compaction. This sediment type was also found in Hole 970A, in the intervals 0–0.6, 134–153, and 192–201 mbsf. Density and porosity variations (Figs. 31, 32) are consistent with the effects of compaction and the differing densities of the sapropels and nannofossil ooze layers.

Discrete-sample *P*-wave and Shear Strength Measurements

Horizontal and vertical *P*-wave velocities measured with the digital sonic velocimeter show a generally increasing trend with depth in Hole 970A (Table 10, Fig. 33). Owing to an increase in sediment cohesiveness, the measurement method was switched from DSV 1 to DSV 3 at 39 mbsf. The DSV 3 measurements show a large scatter. The presence of voids and the heterogenous matrix in the mud volcano sediments made DSV and vane-shear measurements difficult to obtain. The vane-shear data are presented in Table 11 and Figure 34.

GRAPE Density

MST measurements were made on some cores from Holes 970A through 970D; core recovery and the presence of numerous gas voids and gaps limited the reliability of the MST measurements. The only MST data that appear credible for Site 970 are those from the GRAPE, and these are available for most of the upper 45 m of each hole. GRAPE densities are presented in Figure 35, and the overall trends of the GRAPE density are similar to those observed in the index properties density data. However, a comparison of index properties density measurements (Fig. 31) with GRAPE density suggests that GRAPE measurements in this hole underestimate density, despite application of the Boyce correction (see "Explanatory Notes" chapter, this volume, and the "Physical Properties" section, "Site 967" chapter, this volume).

Thermal Conductivity

Thermal conductivity at Hole 970A was sampled once per section in all cores from Hole 970A (Table 12, Fig. 36). Thermal conductivity values are scattered about a value of 1.4 W/(m · K).

Table 7. Concentration of inorganic, total, and organic carbon, calcium carbonate, total nitrogen, and sulfur in sediments from Site 970.

Core, section, interval (cm)	Depth (mbsf)	Total carbon (%)	Inorganic carbon (%)	Organic carbon (%)	$CaCO_3$ (%)	Nitrogen (%)	Sulfur (%)	C_{org}/N	C_{org}/S
160-970A-									
2H-1, 61–62	8.21	2.68	1.86	0.82	15.5	0.07	0.58	11.3	1.4
3X-CC, 35–36	10.55	2.19	1.71	0.48	14.2	0.07	0.78	7.2	0.6
4X-1, 59–60	18.79	12.82	5.35	7.47	44.6	0.45	2.75	16.8	2.7
4X-1, 75–76	18.95		6.38		53.1				
4X-CC, 27–28	19.63		6.96		58.0				
5X-CC, 10–11	27.9	2.20	1.85	0.35	15.4	0.06	1.05	5.5	0.3
6X-1, 59–60	37.99		1.87		15.6				
7X-1, 50–51	47.6	2.36	1.84	0.52	15.3	0.07	1.25	7.8	0.4
9X-1, 36–37	66.66	2.80	2.23	0.57	18.6	0.06	0.39	8.8	1.5
10X-1, 50–51	76.5	1.69	1.69	0.00	14.1	0.04	0.48		
11X-CC, 35–36	86.05		8.93		74.4				
13X-1, 31–32	105.41	1.53	1.06	0.47	8.8	0.07	0.72	6.8	0.7
14X-1, 34–35	115.14	2.17	1.74	0.43	14.5	0.06	0.98	7.0	0.4
15X-2, 50–51	126.29	2.42	1.95	0.47	16.2	0.06	0.57	8.4	0.8
16X-2, 50–51	136		5.97		49.7				
16X-3, 50–51	137.5		5.65		47.1				
17X-1, 41–42	144.01	13.99	5.58	8.41	46.5	0.50	3.52	16.9	2.4
17X-1, 70–71	144.3	13.32	6.31	7.01	52.6	0.40	3.88	17.7	1.8
17X-2, 47–48	145.57		5.48		45.6				
17X-3, 7–8	146.67	9.25	5.90	3.35	49.1	0.23	3.82	14.6	0.9
18X-1, 50–51	153.7	3.90	3.58	0.32	29.8	0.04	1.84	7.9	0.2
18X-2, 99–100	155.49	3.37	2.77	0.60	23.1	0.05	1.88	12.4	0.3
19X-2, 53–54	164.83	2.15	2.10	0.05	17.5	0.04	1.31		
19X-3, 45–46	166.13	3.06	2.61	0.45	21.7	0.05	1.58	9.7	0.3
20X-2, 52–53	174.52	2.83	2.30	0.53	19.2	0.05	0.65	10.6	0.8
21X-1, 44–45	182.54	3.86	3.56	0.30	29.7	0.04	0.78	7.6	0.4
21X-3, 23–24	185.33	3.34	2.91	0.43	24.2	0.05	1.19	8.6	0.4
22X-1, 70–71	192.4		6.14		51.1				
22X-1, 134–135	193.04	24.99	2.38	22.61	19.8	1.06	6.09	21.3	3.7
22X-2, 9–10	193.29	15.39	3.39	12.00	28.2	0.65	4.82	18.5	2.5
22X-2, 75–76	193.95	19.67	2.46	17.21	20.5	0.92	5.58	18.7	3.1
22X-2, 118–119	194.38	17.35	2.39	14.96	19.9	0.76	5.16	19.6	2.9
22X-3, 56–57	195.26		7.37		61.4				
160-970B-									
1H-1, 92–93	0.92	9.68	6.25	3.43	52.1	0.23	3.34	14.9	1.0
1H-2, 19–20	1.69	11.34	5.41	5.93	45.1	0.36	3.28	16.5	1.8
1H-2, 88–89	2.38	9.82	6.69	3.13	55.7	0.21	2.45	14.9	1.3
2H-2, 20–21	10.2		4.94		41.2				
2H-3, 67–68	11.3		8.25		68.7				
2H-4, 58–59	12.67	9.60	6.72	2.88	56.0	0.18	1.29	16.0	2.2
2H-5, 101–102	14.48	13.13	4.88	8.25	40.7	0.38	5.56	21.7	1.5
2H-5, 126–127	14.73	8.88	5.59	3.29	46.6	0.22	2.71	15.0	1.2
2H-6, 20–21	15.12		5.61		46.7				
2H-8, 24–25	17.99	8.39	5.75	2.64	47.9	0.19	0.81	13.9	3.3
3H-4, 58–59	24.08	9.04	4.88	4.16	40.7	0.26	5.29	16.0	0.8
3H-5, 17–18	25.17	12.46	6.80	5.66	56.6	0.32	4.31	17.7	1.3
3H-5, 101–101	26.01	12.55	4.94	7.61	41.2	0.41	4.33	18.6	1.8
3H-6, 88–89	27.38	12.26	6.13	6.13	51.1	0.33	3.48	18.6	1.8
3H-CC, 15–16	28.81	10.90	6.35	4.55	52.9	0.29	2.04	15.7	2.2
4H-2, 70–71	30.7		4.37		36.4				
4H-2, 148–149	31.48	9.93	6.72	3.21	56.0	0.20	2.92	16.0	1.1
4H-3, 23–24	31.73	9.14	6.56	2.58	54.6	0.19	4.29	14.0	0.6
4H-3, 93–94	32.43	12.66	5.59	7.07	46.6	0.40	5.58	17.8	1.3
4H-4, 100–101	34	7.61	1.69	5.92	14.1	0.34	5.08	17.2	1.2
4H-5, 8–9		34.58	16.07	0.43	15.64	3.6	0.85	12.85	18.5
4H-5, 70–71	35.2		6.46		53.8				
4H-6, 59–60	36.59	10.59	5.42	5.17	45.1	0.35	5.98	14.7	0.9
5H-1, 8–9		38.08	8.87	5.40	3.47	45.0	0.23	2.53	15.1
5H-1, 30–31	38.3	14.35	1.19	13.16	9.9	0.64	4.73	20.6	2.8
5H-1, 63–64	38.63	19.80	1.74	18.06	14.5	0.87	5.55	20.8	3.3
5H-2, 31–32	39.54		5.91		49.2				
5H-3, 30–31	41.03		5.89		49.1				
5H-3, 117–118	41.9	15.00	3.69	11.31	30.7	0.60	4.74	18.9	2.4
5H-4, 60–61	42.83		3.61		30.1				
5H-5, 107–108	44.8	12.66	5.26	7.40	43.8	0.42	4.53	17.6	1.6
160-970C-									
1H-2, 60–61	2.1	2.76	2.45	0.31	20.4	0.06	0.10	4.9	3.0
2H-3, 39–40	8.01		2.14		17.8				
4X-1, 2–3	12.67		1.51		12.6				
160-970D-									
1H-1, 75–76	0.75	1.30	1.21	0.09	10.1	0.04	0.10	2.5	0.9
1H-3, 93–94	3.93	1.66	1.66	0.00	13.8	0.05	0.00		
2H-1, 35–36	5.15		1.80		15.0				
2H-4, 35–36	9.65	2.23	1.86	0.37	15.5	0.07	1.04	5.3	0.4
2H-7, 35–36	14.15		2.00		16.7				
3H-2, 69–70	16.49	3.20	2.88	0.32	24.0	0.07	0.99	4.9	0.3
3H-4, 69–70	19.49		1.94		16.2				

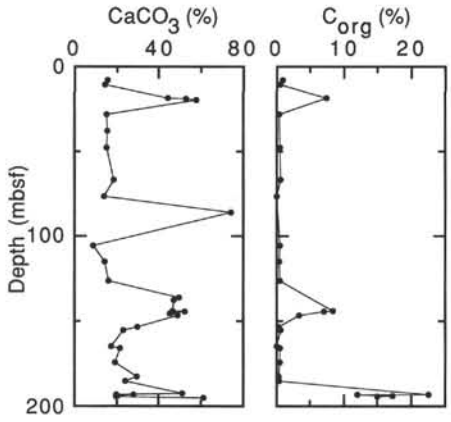

Figure 30. Downhole distribution of calcium carbonate and organic carbon concentrations in sediments from Hole 970A.

DOWNHOLE MEASUREMENTS

Logging Operations and Quality of Logs

At Site 970, we acquired a full suite of log data by using the split Quad combination (seismic-stratigraphic and litho-porosity) and the Formation Microscanner tool strings (see "Explanatory Notes" chapter, this volume). We decided to run the Quad combination in two parts because of uncertainty about hole conditions in such a difficult environment as a mud volcano. After running the seismic-stratigraphic string without any difficulties, we ran the litho-porosity string with the Lamont-Doherty temperature logging tool attached at the bottom. After coring and drilling operations were completed in Hole 970A, the borehole was conditioned with sepiolite drilling mud mixed with seawater. The base of the BHA was set at 88.8 mbsf and pulled up to 64.25 mbsf. We logged between 202.2 and 64.25 mbsf.

Table 13 summarizes the intervals logged with each tool string. The logs are of good quality, although the caliper measurements indicate a borehole washout zone (i.e., hole diameter >40 cm) over most of the lowermost interval at 133–202.2 mbsf (Fig. 37), which affected the quality of some of the measurements sensitive to hole condition, notably the density log. The sonic log is generally of good quality but needs reprocessing for the uppermost part (64.25–133 mbsf), where cycle skips occurred.

The two passes of the FMS tool string provided high-resolution resistivity images of the borehole wall, measurements of the three vector components of the local magnetic field (GPIT), and the borehole inclination, deviation, and diameter in two orthogonal directions. The FMS images are of low quality where the borehole diameter exceeded 38 cm because of poor contact of the FMS pads with the borehole wall.

Results and Interpretation

Two main log units are identified on the basis of the log response. These units coincide with those differentiated independently from the recovered core (see "Lithostratigraphy" section, this chapter). The log units and subunits are shown in Figure 38.

Log Unit 1 (64.5–134 mbsf)

The most striking feature within log Unit 1 is the homogeneity and low variability of the log values. This indicates a rather homogeneous lithology, observed as well in the recovered materials (see "Lithostratigraphy" section, this chapter). The lithology has been defined as matrix-supported clast-rich debris-flow deposits. The caliper logs indicate relatively good hole conditions throughout the section, which suggests that these deposits are well consolidated. Furthermore, the density values (in the range of 1.9–2.1 g/cm^3) indicate a rather dense material at this depth.

Unit 1 can be divided into intervals with a similar log response that are bounded by sharp changes in the log values of the PEF, density, resistivity, natural radioactivity, and neutron porosity. Poor recovery in the logged section of Unit 1 prevents correlation of the logs with the cores and identification of the layers separating the individual intervals. Because the unit is interpreted as the result of episodic debris flows (see "Lithostratigraphy" section, this chapter), it seems that the sharp changes in the log values most likely represent boundaries between different flows. These boundaries are located at 68, 82.5, 97, 106, 115, and 128 mbsf. At the base of Unit 1, a sharp decrease in all the log values and a considerable enlargement of the hole indicate a major lithologic and textural change that defines the unit boundary. The FMS images indicate that the sedimentary facies of Unit 1 is a polymictic breccia-like material. A highly resistive boulder with a diameter of about 55 cm was observed at 131 mbsf.

Log Unit 2 (133–202 mbsf)

Both gradual and abrupt changes in composition and layering are inferred from the fluctuations of log values in Unit 2. On the FMS images this unit shows layering throughout. Intervals of well-bedded material alternate with others where gradational changes between highly resistive (coarser) material and less resistive (finer) material were recognized.

The five subunits identified on the basis of the log response observed in the set of standard (Quad combination) logs denote variations in both composition and internal structure. They are found at the following depths: Subunit 2A (134–153.5 mbsf), Subunit 2B (153.5–163.5 mbsf), Subunit 2C (163.5–183.5 mbsf), Subunit 2D (183.5–196 mbsf), and Subunit 2E (from 196 mbsf to the bottom of the logged interval). The boundaries between Subunits 2A/2B, 2B/2C, and 2D/2E are sharp. These features are shown in Figure 38. The sediments recovered at depths corresponding to Subunit 2A and Subunit 2E have been characterized as nannofossil ooze and sapropels, and those from the depth interval of Subunits 2B, 2C, and 2D as matrix-supported clast-rich debris-flow deposits (see "Lithostratigraphy" section, this chapter). The nature of the changes that give rise to the different log response within the matrix-supported clast-rich debris-flow deposits is not directly correlatable with the core descriptions, but might be related to internal textures and structures of the sediments or to diagenesis.

Gradational changes in log values over 3–5-m intervals within Subunit 2C suggest the presence of graded sequences. The high radioactivity observed in Subunits 2A and 2B results mainly from uranium, suggesting organic-rich layers, and it is probably related to sapropel occurrences.

Temperature Logging Tool

Borehole temperature measurements were recorded in Hole 970A using the Lamont-Doherty TLT during run 2 with the Quad combination string. Downhole and uphole profiles were acquired. The tool string stayed at the bottom of the hole for a few minutes to determine the bottom-hole temperature.

Figure 39 shows the fast- and the slow-thermistor temperatures for the downhole and uphole runs. The temperature of the borehole was still equilibrating. The bottom-hole temperature varied between 14.9° and 15.15°C. The anomalies in the downhole profile indicate zones where water flows into the borehole from the formation (see Table 14 for precise locations). There is no evidence from the other logs for a systematic link between these fluctuations and changes in the properties of the formation. Further processing of the recorded temperature data together with operational data, such as the time of the last circulation of drilling fluids, should facilitate a more detailed interpretation.

Table 8. Results of Rock-Eval analysis for Site 970.

Core, section, interval (cm)	Depth (mbsf)	S_1 (mg/g)	S_2 (mg/g)	S_3 (mg/g)	TOC (%)	PC	HI	OI	T_{max} (°C)	PI	S_2/S_3
160-970A-											
4X-1, 59–60	18.79	5.37	20.94	1.76	7.47	2.18	280	24	414	0.20	11.90
17X-1, 41–42	144.01	5.14	26.34	1.34	8.41	2.61	313	16	419	0.16	19.66
17X-1, 70–71	144.30	6.83	23.15	1.45	7.01	2.49	330	21	412	0.23	15.97
17X-3, 7–8	146.67	1.34	8.96	0.76	3.35	0.85	267	23	419	0.13	11.79
22X-1, 134–135	193.04	19.69	85.55	2.46	22.61	8.73	378	11	427	0.19	34.78
22X-2, 9–10	193.29	9.66	44.63	1.65	12.00	4.51	372	14	422	0.18	27.05
22X-2, 75–76	193.95	16.09	62.24	2.19	17.21	6.50	362	13	417	0.21	28.42
22X-2, 118–119	194.38	12.07	52.98	1.92	14.96	5.40	354	13	421	0.19	27.59
160-970B-											
2H-4, 58–59	12.67	1.38	7.38	0.86	2.88	0.73	256	30	420	0.16	8.58
2H-5, 101–102	14.48	5.79	29.26	1.71	8.25	2.91	355	21	422	0.17	17.11
2H-5, 126–127	14.73	1.21	7.71	0.91	3.29	0.74	234	28	423	0.14	8.47
2H-8, 24–25	17.99	1.30	5.16	0.89	2.64	0.54	195	34	415	0.20	5.80
4H-2, 148–149	31.48	1.04	6.80	0.87	3.21	0.65	212	27	423	0.13	7.82
4H-3, 23–24	31.73	1.12	5.35	0.82	2.58	0.54	207	32	413	0.17	6.52
4H-3, 93–94	32.43	4.99	22.08	1.50	7.07	2.25	312	21	418	0.18	14.72
4H-4, 100–101	34.00	2.93	17.78	0.91	5.92	1.72	300	15	419	0.14	19.54
4H-5, 8–9	34.58	11.46	45.63	2.01	15.64	4.74	292	13	412	0.20	22.70

Notes: TOC = total organic carbon; PC = petroleum potential as pyrolyzable carbon; HI = hydrogen index; OI = oxygen index; PI = production index; see the "Explanatory Notes" chapter (this volume) for units for these parameters.

Table 9. Index properties measured in cores from Site 970.

Core, section, interval (cm)	Depth (mbsf)	Water content (wt%)	Porosity (vol%)	Bulk density (g/cm^3)		Grain density (g/cm^3)		Dry density (g/cm^3)	
				Method B	Method C	Method B	Method C	Method B	Method C
160-970A-									
1H-1, 71–73	0.71	34.18	60.70	1.82	1.76	3.05	2.79	1.20	1.16
1H-2, 71–73	2.21	30.50	54.17	1.82	1.81	2.76	2.72	1.26	1.26
1H-3, 70–72	3.70	27.79	52.22	1.93	1.87	2.91	2.73	1.39	1.35
1H-4, 75–77	5.25	27.10	51.46	1.95	1.88	2.92	2.72	1.42	1.37
1H-5, 61–63	6.61	26.24	50.34	1.97	1.90	2.92	2.74	1.45	1.40
2H-1, 123–125	8.83	37.08	63.24	1.75	1.68	2.99	2.71	1.10	1.06
2H-2, 90–92	10.00	33.81	58.90	1.78	1.74	2.87	2.72	1.18	1.15
3X-CC, 17–19	10.37	25.13	48.05	1.96	1.91	2.82	2.70	1.47	1.43
4X-1, 90–92	19.10	38.42	64.69	1.72	1.67	3.01	2.77	1.06	1.03
4X-CC, 9–11	19.45	33.16	58.04	1.79	1.76	2.86	2.72	1.20	1.17

Only part of this table is reproduced here. The entire table appears on the CD-ROM (back pocket).

SUMMARY AND CONCLUSIONS

An east-northeast–west-northwest transect of four holes was drilled from the flank to the crest of the Milano mud structure, within the Olimpi mud diapir field located on the northern part of the Mediterranean Ridge (150 km south of Crete). The results confirm an origin as a mud volcano rather than a mud diapir. Hole 970A (to 200 mbsf) sampled the mud volcano's outer flank; Hole 970B (to 50 mbsf), approximately 600 m farther from the volcano, examined the most distal effects of mud volcanism; Hole 970C (to 50 mbsf) characterized the nature of the upper flank of the mud volcano; and, finally, Hole 970 D (to 30 mbsf) examined the crestal area.

At the outermost hole (Hole 970B), the sediments comprise interbedded nannofossil oozes, nannofossil clays, and sapropels typical of the regional hemipelagic sedimentation. There are also poorly consolidated thin- to medium-bedded sands and silts. Some intervals are tilted and small normal and reverse faults were noted. This section is dated as early-late Pleistocene.

The outer flank hole (Hole 970A) comprises alternations of mud debris flows and normal hemipelagic sediment. The section begins with pebbly mudstone capped by a thin (<1 m) pelagic interval. This is underlain by thick clast-rich mud debris flows (7.6–134 mbsf), and then by a thin interval of pelagic sediment (134–153 mbsf), which was dated as slightly older than 1.5 Ma to slightly younger than 0.99 Ma. This, in turn, is followed by layered coarse-grained turbidites with mud clasts at the base, together with minor graded sands and silts (153–192 mbsf), and then finally by normal pelagic sediments (192–201 mbsf) dated at 1.75 Ma. Downhole logs, including the FMS, clearly define the main intervals and show that the mud debris flows include numerous clasts of various different lithologies, up to 0.5 m in diameter.

The inner flank and crestal sites (Hole 970C and the top of Hole 970D) recovered mainly "mousselike" (i.e., gaseous) muddy and silty sediments, with evidence of gas hydrates (see below).

A number of different mud volcanic facies are present. The clast-supported facies in the lower part of Hole 970A are interpreted as turbidites and minor debris flows. The predominant extrusive sediment type, however, is well-consolidated matrix-supported, breccia/conglomerate (the traditional "mud breccias"), in which the matrix ranges from silty clay to rare sandy silt, with nannofossils, foraminifers, clay, quartz, and rock fragments. Clasts vary in shape from mainly subangular to subrounded and less commonly angular or rounded. The clast lithologies include poorly consolidated sandstone and siltstone and weakly to well-consolidated calcareous claystone and mudstone, together with calcite- (or locally quartz-) cemented sandstone and siltstone.

Numerous sandstone clasts are mostly litharenites, derived from mainly plutonic igneous and metamorphic source terrains, admixed with shallow-water carbonate (e.g., calcareous algae and polyzoans and pelagic carbonate). Lithoclasts of pelagic carbonate include foraminifers of middle Miocene (Burdigalian-Langhian) age. In addition, some clasts contain nannofossils and planktonic foraminifers of

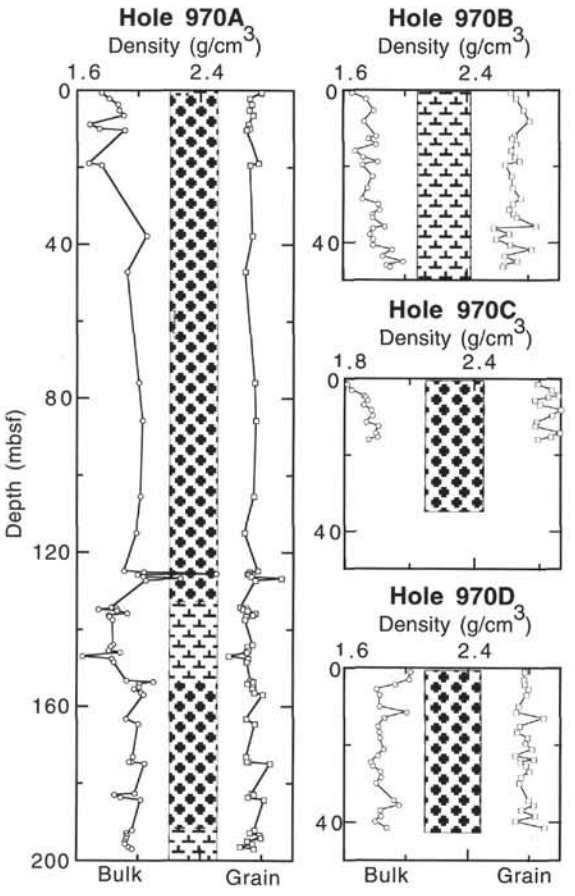

Figure 31. Index properties densities measured in cores from Site 970, shown with lithologic summaries (see "Lithostratigraphy" section, this chapter).

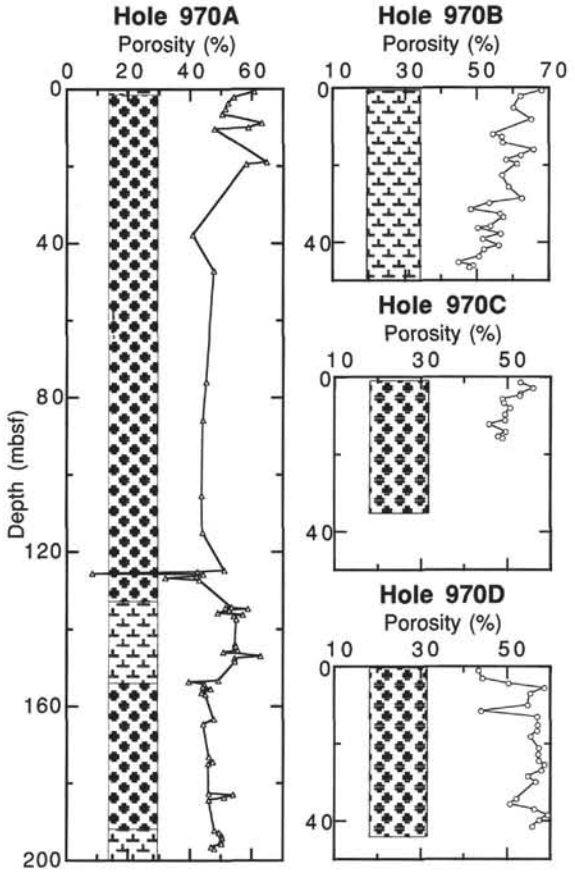

Figure 32. Index properties porosity measured in cores from Site 970, shown with lithologic summaries.

Table 10. Compressional wave velocity measured in split cores from Holes 970A and 970B.

Core, section, interval (cm)	Depth (mbsf)	Measurement type	Velocity (km/s)
160-970A-			
1H-1, 65.2	0.65	DSV 1	1.56
1H-1, 66.1	0.66	DSV 2	1.30
1H-1, 70.5	0.71	DSV 2	1.61
1H-2, 54.6	2.05	DSV 1	1.61
1H-2, 70.5	2.21	DSV 2	1.55
1H-3, 52.6	3.53	DSV 1	1.64
1H-3, 53.0	3.53	DSV 2	1.61
1H-5, 117.7	7.18	DSV 2	1.69
1H-5, 125.8	7.26	DSV 2	1.67
16X-1, 41.6	134.42	DSV 3	2.18

Note: Direct DSV measurements.

Only part of this table is reproduced here. The entire table appears on the CD-ROM (back pocket).

Eocene and Oligocene age and rare nannofossils of Cretaceous age, again within clasts of Miocene pelagic limestone; brackish-water ostracodes (Messinian or early Pliocene age?) were also observed in a few clasts.

Pore-water salinities in Holes 970A and 970B show a linear increase with depth to approximately twofold seawater values. By contrast, in Holes 970C and 970D, pore-water salinities decrease with depth, which can be explained by the decomposition of clathrates (methane hydrates). Very low sulfate levels in this hole may relate to intense bacterial sulfate reduction.

In Hole 970D, bubbles generated in the mud by decompression contained pure methane in the upper 30 m, but with concentrations several orders of magnitude lower beneath this (to 50 mbsf). Levels of higher hydrocarbons relative to methane increase toward the bottom of the hole, so that the methane/ethane ratio decreased from about 1300 in the top core to 18 in the lowest part (40–50 mbsf). Carbonate contents range from 40% to 60% in the pelagic intervals, to typically 15% within the matrix of the mud breccias, and from 20% to 30% within the stratified clastic sediments in the lower part of Hole 970A. Organic carbon values in the mud matrix are low (approximately 0.5%).

The Milano mud volcano became active at about 1.75 Ma or earlier. Stratified turbidites and debris flows record relatively early mud volcanism. Mud flows were localized around the eruptive center on the transect studied. Seismic reflectors around the mud volcano dip inward and imply progressive subsidence, which perhaps permitted the ponding of mud debris flows. Normal pelagic sediments accumulated around the mud volcano during the Pleistocene, and are interbedded with silts and sands that were possibly shed as turbidites from the crestal area. Hemipelagic sediments interdigitate with mud debris flows on the flanks, whereas more silty and mousselike sediments with clathrates characterize the crestal area.

REFERENCES

Brown, K., and Westbrook, G.K., 1988. Mud diapirism and subcretion in the Barbados Ridge accretionary complex: the role of fluids in accretionary processes. *Tectonics,* 7:613–640.

Brumsack, H.-J., Zuleger, E., Gohn, E., and Murray, R.W., 1992. Stable and radiogenic isotopes in pore waters from Leg 127, Japan Sea. *In* Pisciotto, K.A., Ingle, J.C., Jr., von Breymann, M.T., Barron, J., et al., *Proc. ODP,*

Sci. Results, 127/128 (Pt. 1): College Station, TX (Ocean Drilling Program), 635–650.

Camerlenghi, A., Cita, M.B., Della Vedova, B., Fusi, N., Mirabile, L., and Pellis, G., 1995. Geophysical evidence of mud diapirism on the Mediterranean Ridge accretionary complex. *Mar. Geophys. Res.,* 17:115–141.

Camerlenghi, A., Cita, M.B., Hieke, W., and Ricchiuto, T.S., 1992. Geological evidence for mud diapirism on the Mediterranean Ridge accretionary complex. *Earth Planet. Sci. Lett.,* 109:493–504.

Cita, M.B., and Camerlenghi, A., 1990. The Mediterranean Ridge as an accretionary prism in collision context. *Mem. Soc. Geol. Ital.,* 45:463–480.

Cita, M.B., Erba, E., Lucchi, R., van der Meer, R., Pott, M., and Nieto, L., 1994. Bottom sampling in the Olimpi mud volcano area. *In* Limonov, A.F., Woodside, J.M., and Ivanov, M.K. (Eds.), *Mud Volcanism in the Mediterranean and Black Seas and Shallow Structure of the Eratosthenes Seamount.* UNESCO Rep. Mar. Sci., 64:89–107.

Cita, M.B., Ryan, W.B.F., and Paggi, L., 1981. Prometheus mud-breccia: an example of shale diapirism in the Western Mediterranean Ridge. *Ann. Geol. Pays Hellen.,* 30:543–570.

Henry, P., LePichon, X., Lallemant, S., Foucher, J.-P., Westbrook, G., and Hobart, M., 1990. Mud volcano field seaward of the Barbados accretionary complex: a deep-towed side scan sonar survey. *J. Geophys. Res.,* 95:8917–8929.

Katz, D.L., Cornell, D., Kobayashi, R., Poettmann, F.H., Vary, J.A., Elenblass, J.R., and Weinaug, C.F., 1959. *Handbook of Natural Gas Engineering:* New York (McGraw-Hill).

Limonov, A.F., Woodside, J.M., and Ivanov, M.K. (Eds.), 1994. *Mud Volcanism in the Mediterranean and Black Seas and Shallow Structure of the Eratosthenes Seamount.* UNESCO Rep. Mar. Sci., 64.

Lowe, D.R. 1982. Depositional models with special reference to the deposits of high density turbidity currents. *J. Sediment. Pet.,* 5:879–897.

Manheim, F.T., and Sayles, F.L., 1974. Composition and origin of interstitial water of marine sediments based on deep sea drilled cores. *In* Goldberg, E.D. (Ed.), *The Sea* (Vol. 5): New York (Wiley Interscience), 527–568.

Prior, D.B., Doyle, E.H., and Kaluza, M.J., 1989. Evidence of sediment eruption on deep sea floor, Gulf of Mexico. *Science,* 243:517–519.

Staffini, F., Spezzaferri, S., and Aghib, F., 1993. Mud diapirs of the Mediterranean Ridge: sedimentological and micropalaeontological study of the mud breccia. *Riv. Ital. Paleontol. Stratigr.,* 99:225–254.

Volgin, A.V., and Woodside, J.M., in press. Sidescan sonar images of mud volcanoes from the Mediterranean Ridge: causes of variation in backscatter intensity. *Mar. Geol.,* Spec. Iss.

Westbrook, G.K., Carson, B., Musgrave, R.J., et al., 1994. *Proc. ODP, Init. Repts.,* 146 (Pt. 1): College Station, TX (Ocean Drilling Program).

Westbrook, G.K., and Smith, M.J., 1983. Long décollements and mud volcanoes: evidence from the Barbados Ridge Complex for the role of high pore-fluid pressure in the development of an accretionary complex. *Geology,* 11:279–283.

Ms160IR-111

NOTE: Core-description forms ("barrel sheets") and core photographs can be found in Section 5, beginning on page 535. Forms containing smear-slide data can be found in Section 6, beginning on page 951. Color reflectance, physical properties, chemistry, and thin-section data are presented on the CD-ROM (back pocket).

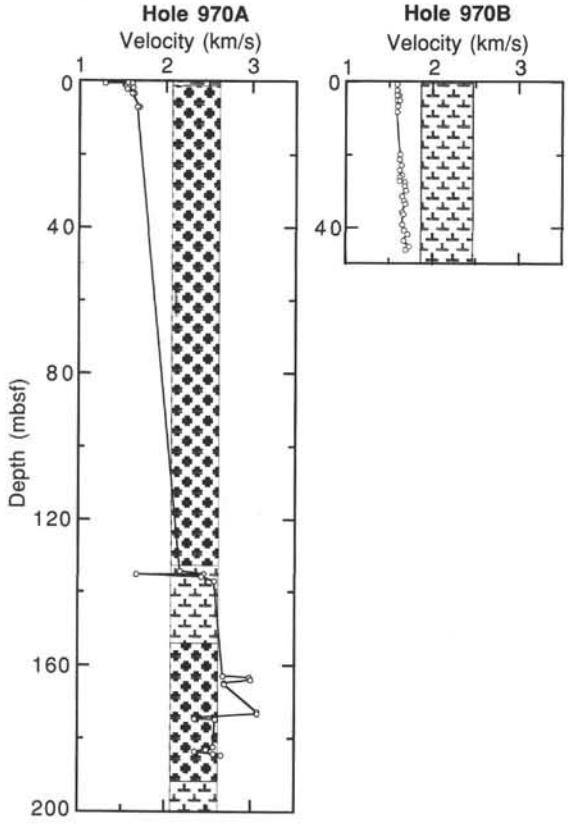

Figure 33. *P*-wave velocity measured in cores from Site 970, shown with lithologic summaries.

Table 11. Vane shear strength measured in split cores from Holes 970A and 970B.

Core, section, interval (cm)	Depth (mbsf)	Strength (kPa)
160-970A-		
1H-1, 71.20	0.71	8.10
1H-2, 21.90	1.72	12.80
1H-2, 77.00	2.27	14.30
1H-2, 132.50	2.83	24.90
1H-3, 41.70	3.42	34.00
1H-3, 90.20	3.90	49.20
1H-3, 124.40	4.24	18.70
1H-4, 114.40	5.64	26.60
1H-5, 48.50	6.49	45.30
1H-5, 110.00	7.10	33.60

Only part of this table is reproduced here. The entire table appears on the CD-ROM (back pocket).

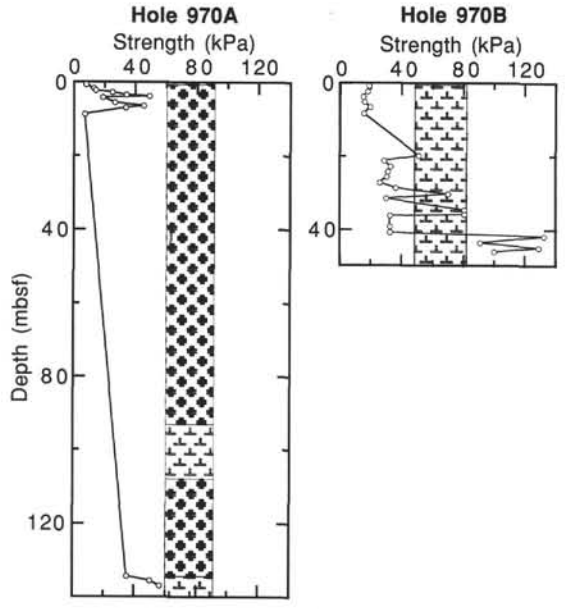

Figure 34. Vane shear strength measured in cores from Site 970, shown with lithologic summaries.

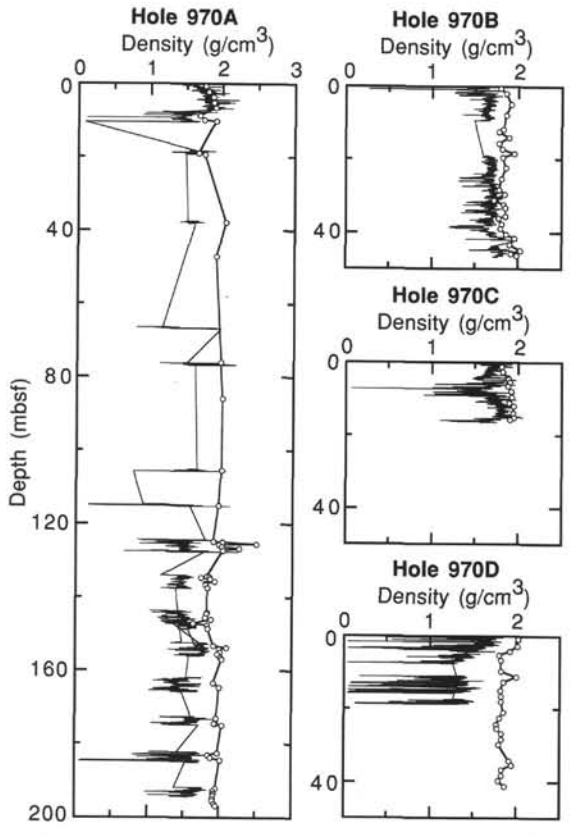

Figure 35. Density measured in cores from Site 970 using the GRAPE component of the MST, shown with index property bulk density (connected open symbols).

Table 12. Thermal conductivity measured in APC cores from Holes 970A and 970B.

Core, section, interval (cm)	Depth (mbsf)	Thermal conductivity (W/[m · K])
160-970A-		
1H-1, 50	0.50	1.225
1H-2, 50	2.00	1.253
1H-3, 50	3.50	1.680
1H-4, 50	5.00	1.569
1H-5, 50	6.50	1.260
2H-1, 50	8.10	1.152
2H-2, 40	9.50	1.025
4X-1, 85	19.05	1.908

Only part of this table is reproduced here. The entire table appears on the CD-ROM (back pocket).

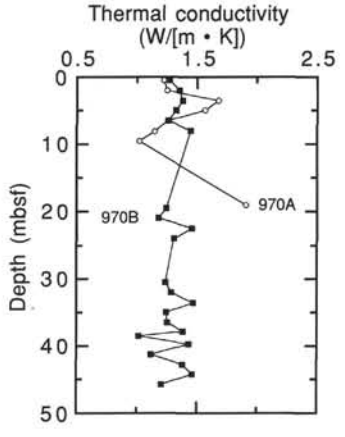

Figure 36. Thermal conductivity measured in cores from Holes 970A and 970B.

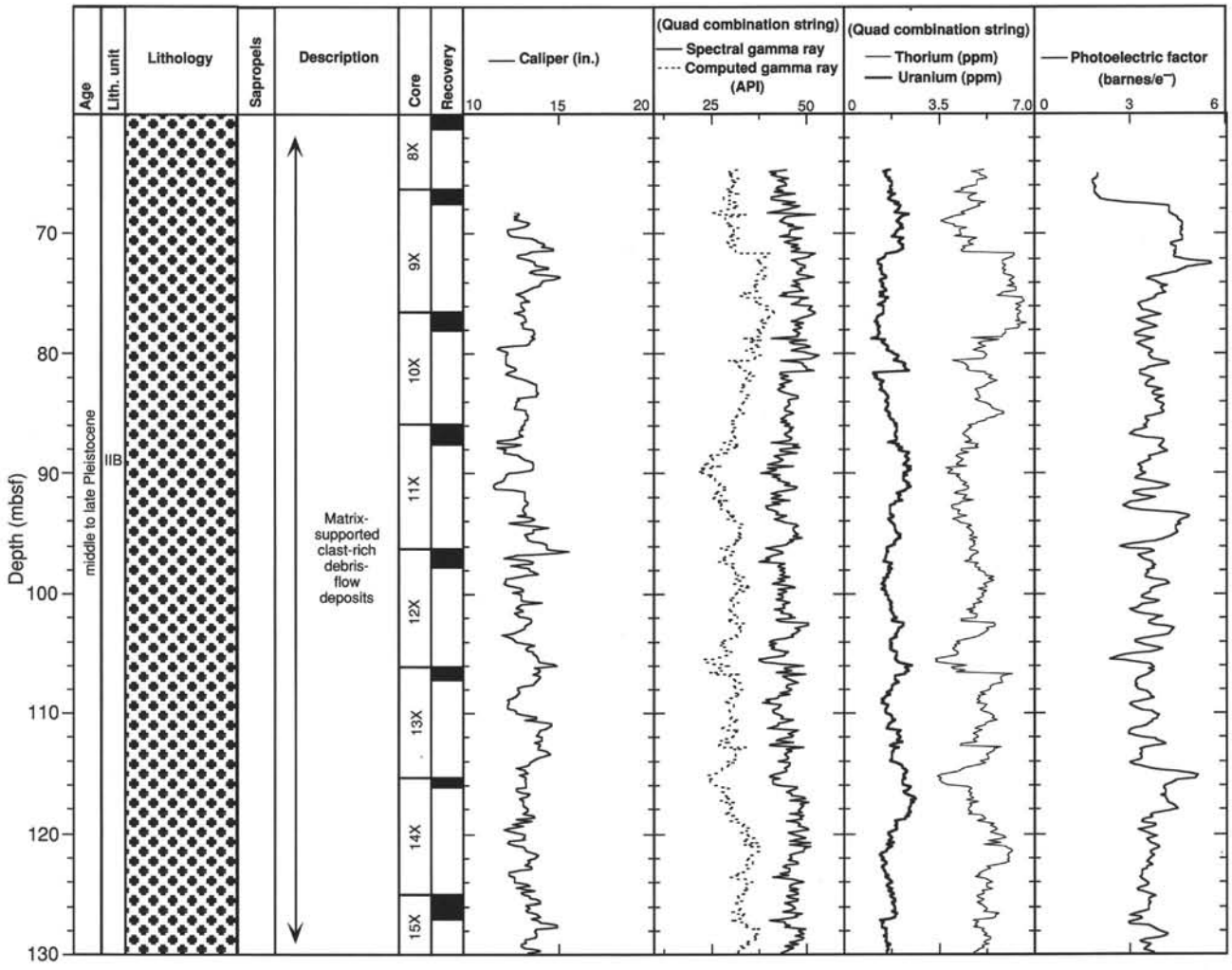

Figure 37. Hole 970A Quad combination tool and FMS (4-arm) caliper results.

Table 13. Hole 970E logged depth intervals for the three tool strings.

String	Run	Open–hole depth (mbsf)	Open–hole depth (mbrf)	In-pipe depth (mbsf)	In-pipe depth (mbrf)	Tools
Seismic-stratigraphic	Down	88.8–180.4	2175.7–2267.3	42.6–88.8	2129.5–2175.7	NGT/SDT/DIT/TLT
	Up 1	201.1–62	2288–2148.9	62–0	2148.9–2086.9	
	Up 2 (repeat section)	200.9–113.3	2287.8–2200.2			
Litho-porosity	Up 1	199.3–62	2286.2–2148.9	62–50.2	2148.9–2137.1	NGT/HLDT/CNT/TLT
	Up 2 (repeat section)	138.4–81	2225.3–2167.9			
FMS	Up 1	199.6–63.2	2286.5–2150.1			NGT/GPIT/FMS
	Up 2	202.5–62	2289.4–2148.9	62–50.7	2148.9–2137.6	

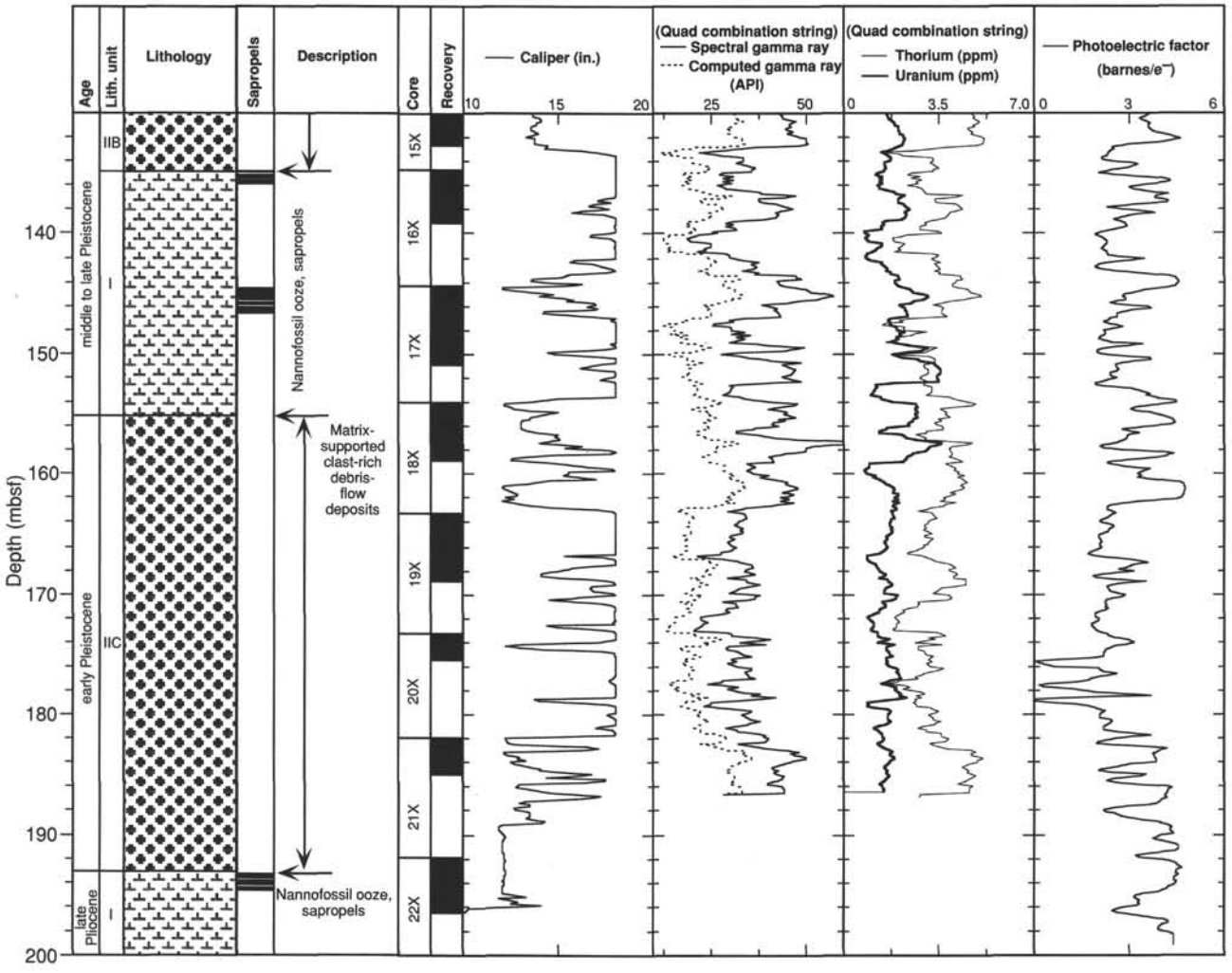

Figure 37 (continued).

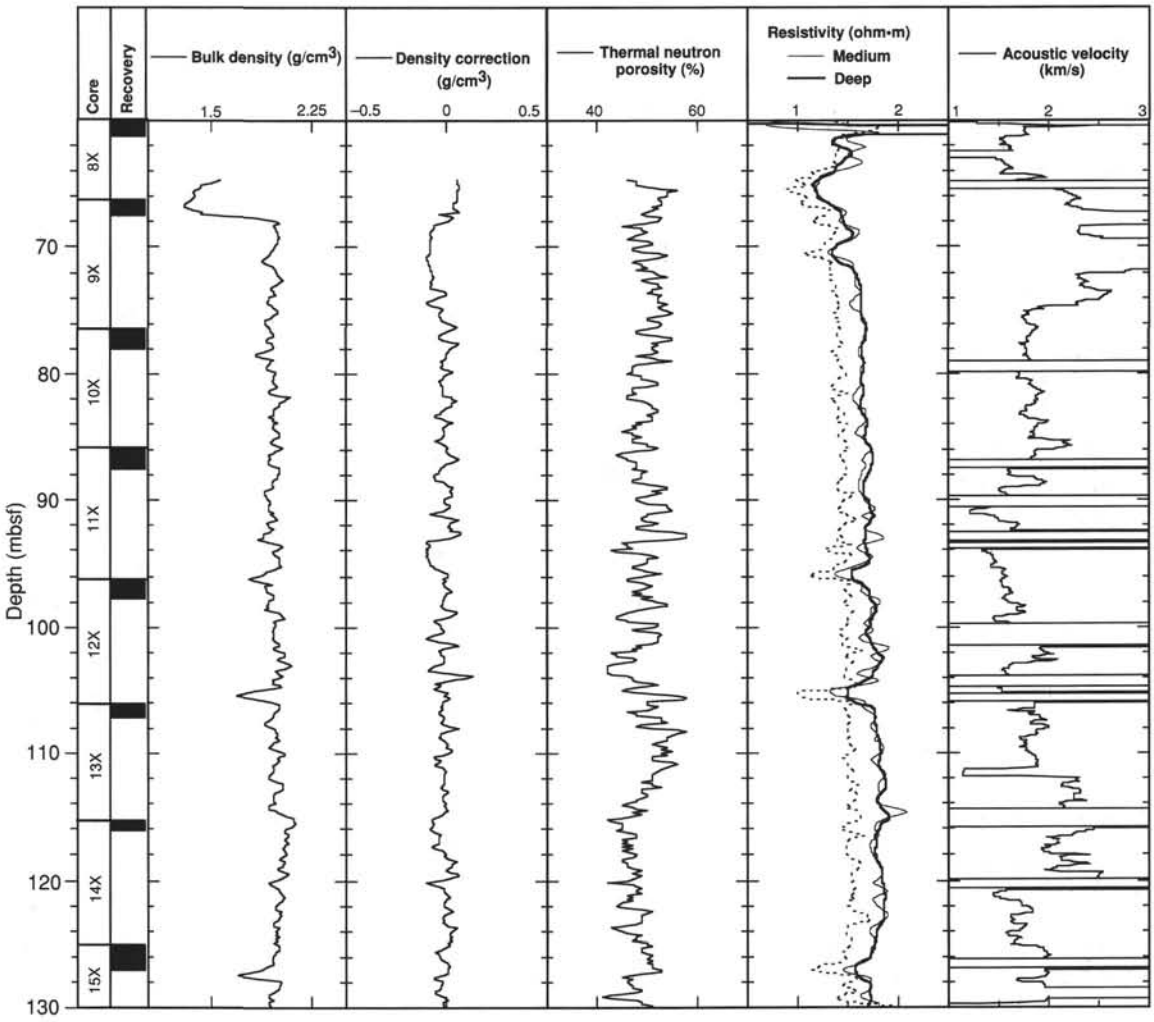

Figure 37 (continued).

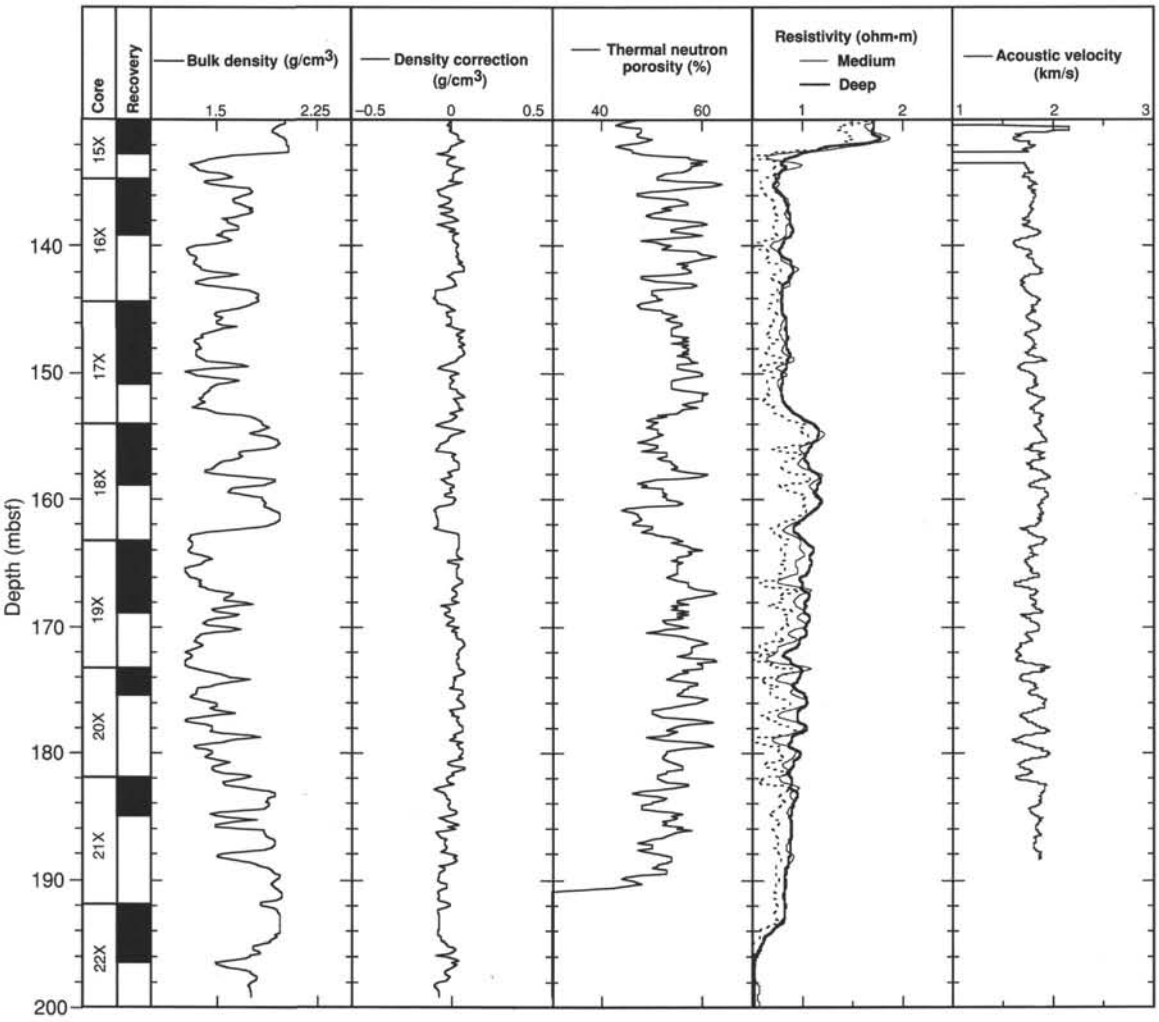

Figure 37 (continued).

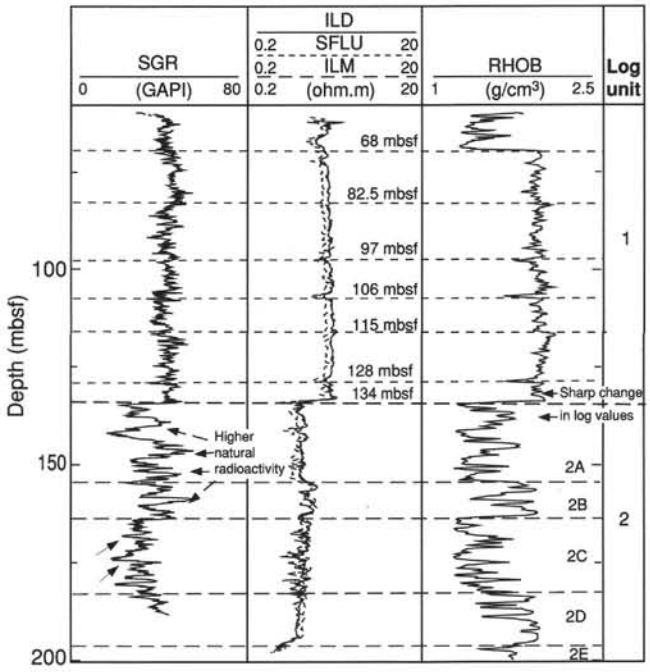

Figure 38. Log Units 1 and 2 in Hole 970A. The natural gamma-ray radioactivity (SGR), resistivity (ILD, SFLU, ILM), and density (RHOB) logs show the significant features interpreted in the text. The dashed lines within Unit 1 indicate changes attributed to boundaries between episodic flows. The dashed lines within Unit 2 indicate the location of the boundaries between Subunits 2A through 2E.

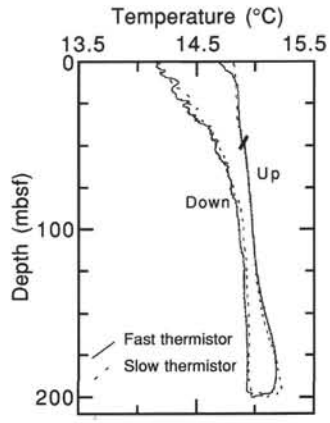

Figure 39. Data from the second run of the temperature logging tool in Hole 970A.

Table 14. Zones of possible water flow.

Zone	Depth (mbsf)
1	1, 5, 12, 20, 25, and 28
2	40, 42, 45, 50, 58, 60, 63, 68, 71, and 85
3	120 and 160

SHORE-BASED LOG PROCESSING

HOLE 970A

Bottom felt: 2086.9 mbrf
Total penetration: 201.4 mbsf
Total core recovered: 50.5 m (25 %)

Logging Runs

Logging string #1: DIT/SDT-LSS/NGT
Logging string #2: HLDT/CNTG/NGT
Logging string #3: FMS/GPIT/NGT

The wireline heave compensator was used to counter ship heave resulting from the mild sea conditions.

Bottom-hole Assembly

The following depths for the BHA are as they appear on the logs after differential depth shift (see **Depth shift** section) and depth shift to the seafloor. As such, there might be a discrepancy with the original depths given by the drillers onboard. Possible reasons for depth discrepancies are ship heave, use of the wireline heave compensator, and drill string and/or wireline stretch.

DIT/SDT-LSS/NGT: BHA at ~60 mbsf.
HLDT/CNTG/NGT: BHA at ~ 59 mbsf.
FMS/GPIT/NGT: did not reach BHA (pass 1).
FMS/GPIT/NGT: BHA at ~ 61 mbsf (pass 2).

Processing

Depth shift: All original logs were interactively depth shifted with reference to the NGT from the DIT/SDT-LSS/NGT run and to the seafloor (2086.2 m).

Gamma-ray processing: The NGT data were processed to correct for borehole size and type of drilling fluid.

Acoustic data processing: The sonic logs were processed to eliminate some of the noise and cycle skipping experienced during the recording.

Quality Control

Data recorded through BHA, such as the NGT and CNTG data above 60 mbsf, should be used only qualitatively because of the attenuation on the incoming signal. An invalid NGT spike was detected at 33-38 mbsf.

The hole diameter was recorded by the hydraulic caliper on the HLDT tool (CALI) and the caliper on the FMS string (C1 and C2).

Details of standard shore-based processing procedures are found in the "Explanatory Notes" chapter (this volume). For further information about the logs, please contact:

Cristina Broglia
Phone: 914-365-8343
Fax: 914-365-3182
E-mail: chris@ldeo.columbia.edu

Elizabeth Pratson
Phone: 914-365-8313
Fax: 914-365-3182
E-mail: beth@ldeo.columbia.edu

Hole 970A: Natural Gamma Ray-Density-Porosity Logging Data

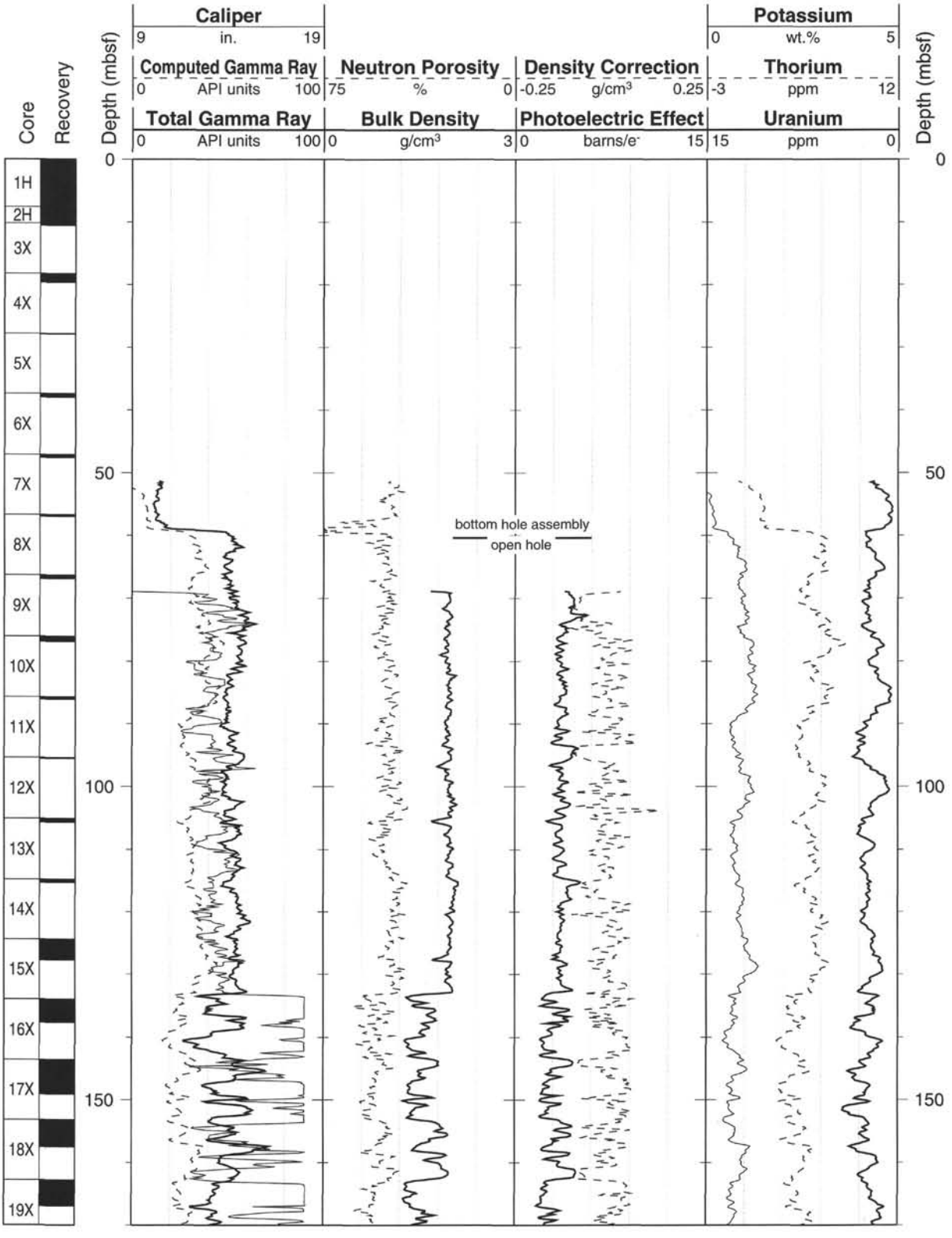

Hole 970A: Natural Gamma Ray-Density-Porosity Logging Data (cont.)

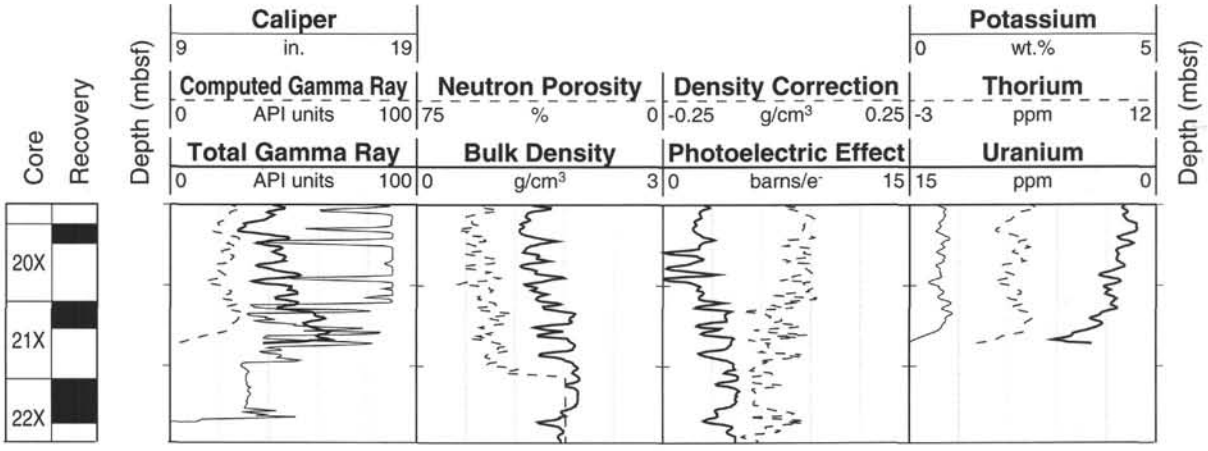

Hole 970A: Natural Gamma Ray-Resistivity-Sonic Logging Data

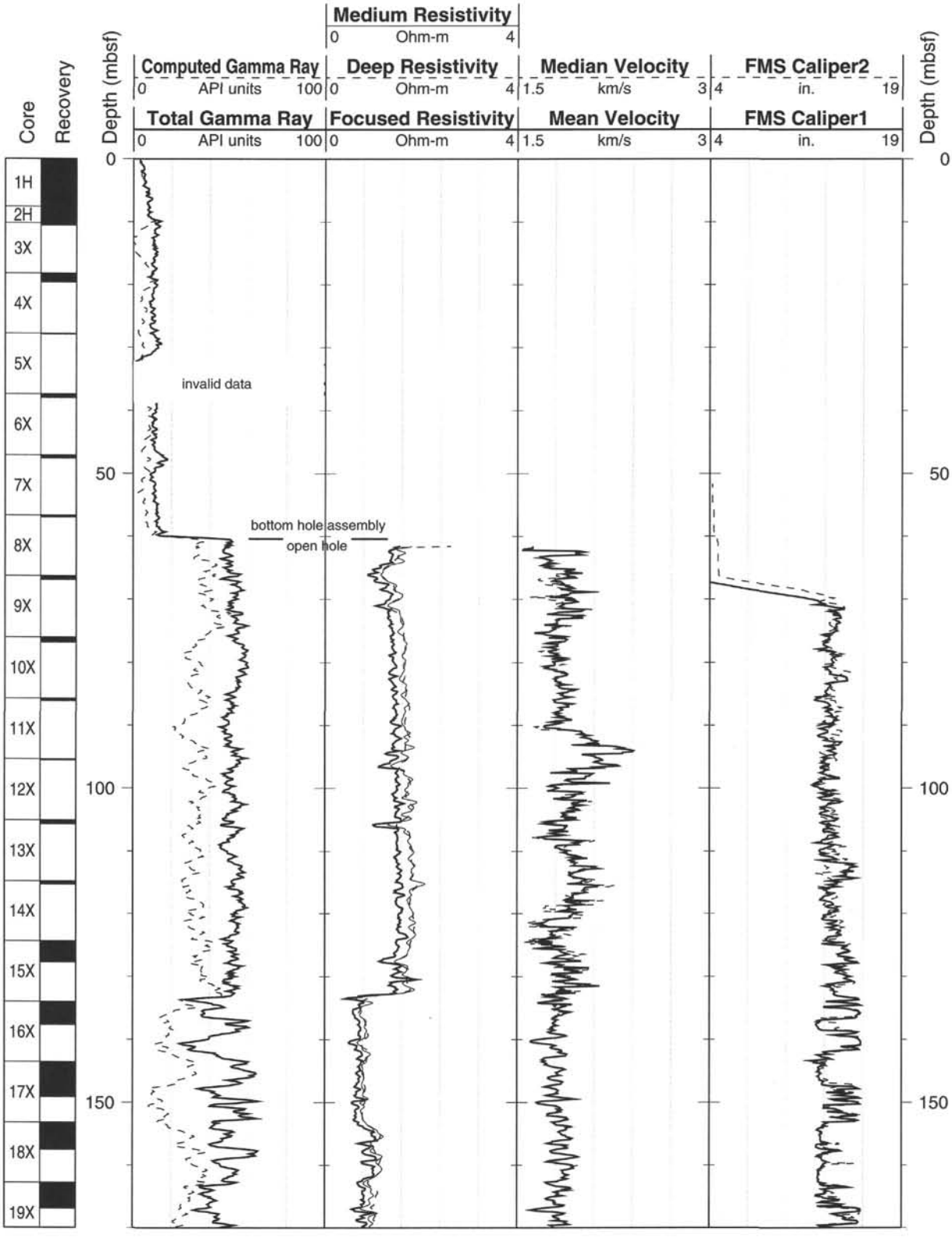

Hole 970A: Natural Gamma Ray-Resistivity-Sonic Logging Data (cont.)